Dichotomy between extracellular signatures of active dendritic chemical synapses and gap junctions

Richa Sirmaur and Rishikesh Narayanan*

Cellular Neurophysiology Laboratory, Molecular Biophysics Unit, Indian Institute of Science, Bangalore, India

*Corresponding author: Rishikesh Narayanan, rishi@iisc.ac.in

Abstract

Local field potentials (LFPs) are compound signals that represent the dynamic flow of information across the brain, which have been historically associated with chemical synaptic inputs. How do gap junctional inputs onto active compartments shape LFPs? We developed methodology to record extracellular potentials associated with different patterns of gap junctional inputs onto conductance-based models. We found that synchronous inputs through chemical synapses yielded a negative deflection in proximal extracellular electrodes, whereas those onto gap junctions manifested a positive deflection. Importantly, we observed extracellular dipoles only when inputs arrived through chemical synapses, but not with gap junctions. Remarkably, hyperpolarization-activation cyclic nucleotide-gated channels, which typically conduct inward currents, mediated outward currents triggered by the fast voltage transition caused by synchronous inputs. With rhythmic inputs at different frequencies arriving through gap junctions, we found strong suppression of LFP power at higher frequencies as well as frequency-dependent differences in the spike phase associated with the LFP, when compared to respective chemical synaptic counterparts. All observed differences in LFP were mediated by the relative dominance of synaptic currents *vs*. voltage-driven transmembrane currents with chemical synapses *vs*. gap junctions, respectively. Our analyses unveil a hitherto unknown role for active dendritic gap junctions in shaping extracellular potentials.

INTRODUCTION

Perpetual ionic movement across membranes and within cells play core physiological roles in the brain. Such ionic movements result in electrical potentials that can be recorded from the extracellular milieu, and are referred to as extracellular field potentials (EFPs). Different types of extracellular potentials, including electroencephalogram, electrocorticogram, and potentials from cell-proximal electrodes, have offered critical insights about brain physiology and have also proved useful in devising brain-computer interfaces (Buzsaki, 2004, 2006; Buzsaki et al., 2012; Einevoll et al., 2013; Obien et al., 2014; Lebedev and Nicolelis, 2017; Pesaran et al., 2018; Pandarinath and Bensmaia, 2022; Halnes et al., 2024). The high-frequency components of cell-proximal extracellular recordings provide spiking information about adjacent neurons. The low-frequency components of these extracellular potentials, referred to as local field potentials (LFP), were traditionally thought to be reflective of currents through synaptic receptors located on different postsynaptic compartments. This synapse-centric view of LFPs was considerably revised after the discovery of active dendrites, to include currents through different ion channels into LFP analyses (Buzsaki et al., 2012; Schomburg et al., 2012; Reimann et al., 2013; Anastassiou et al., 2015; Sinha and Narayanan, 2015; Ness et al., 2016, 2018; Sinha and Narayanan, 2022). However, an important caveat in most LFP analyses is that they are limited to scenarios where synaptic inputs are assumed to be exclusively arriving through chemical synapses that regulate extracellular potentials through transmembrane receptor currents.

Cells in the brain communicate with each other through not just chemical synapses (Dale, 1934; Loewi, 1945; Bullock, 1951), but also through gap junctions (Curtis and Travis, 1951; Furshpan and Potter, 1957; Watanabe, 1958). Connectivity through gap junctions manifests as protoplasmic extensions through specialized molecules implementing a physical continuity between two cells that they connect. Chemical synapses and gap junctions express across different compartments between various cell types across the brain, with mixed connectivity known to manifest between certain cell types (Connors and Long, 2004; Andersen et al., 2006; Pereda, 2014; Connors, 2017; Nagy et al., 2018; Verkhratsky and Nedergaard, 2018). Both electrical and chemical synapses undergo different forms of plasticity and have been implicated in learning and adaptation (Andersen et al., 2006; Neves et al., 2008; O'Brien, 2014; Pereda, 2014; Coulon and Landisman, 2017; Magee and Grienberger, 2020; Vaughn and Haas, 2022).

A fundamental caveat in LFP analyses, therefore, is the omission of inputs arriving through gap junctions, especially onto structures that express an abundance of active mechanisms that mediate transmembrane currents. Incorporation of gap junctional inputs into LFP analyses becomes essential especially because of the several physiological roles played by gap junctions, including in bolstering burst firing and synchronization in different oscillatory bands (Christie et al., 1989; Kepler et al., 1990; Sherman and Rinzel, 1992; Draguhn et al., 1998; Skinner et al., 1999; Alvarez

et al., 2002; Traub et al., 2003; Bennett and Zukin, 2004; Kopell and Ermentrout, 2004; Traub et al., 2011; Connors, 2017). The extracellular potential associated with chemical synapses on a passive membrane would reflect the transmembrane synaptic current as well as the capacitive and leak currents driven by the voltage response to the synaptic current. However, for chemical synapses on an active structure, currents driven by the voltage response would also include all the voltage- and calcium-gated ion channels on the membrane. Unlike chemical synapses, gap junctions do not manifest a transmembrane synaptic current. When postsynaptic structures were considered to be passive, gap junctional impact on field potentials was considered to be indirect through modulation of neural excitability (Halnes et al., 2024). This view, however, needs marked revision to account for the active nature of dendrites (Johnston and Narayanan, 2008; Major et al., 2013; Stuart and Spruston, 2015) and other compartments (Traub and Bibbig, 2000; Traub et al., 2012; Verkhratsky and Nedergaard, 2018) that receive gap junctional inputs.

Analyses of extracellular potentials with gap junctions on active structures must explicitly account for the several transmembrane currents, including the capacitive, leak, and all active currents driven by voltage response to the gap junctional current, towards addressing several important questions. How do similar kinds of inputs arriving through chemical synapses *vs*. gap junctions impact extracellular potentials? What contributions do active structures receiving chemical synapses *vs*. gap junctions make to extracellular potentials? How does the absence of receptor transmembrane current with gap junctional inputs alter potentials across different cell-proximal extracellular electrode locations? Are there differences between the spectral power of extracellular potentials associated with oscillatory inputs arriving onto active or passive structures through chemical synapses *vs*. gap junctions? How does the chemical *vs*. electrical nature of synaptic input alter the relationship between extracellular voltages and intracellular voltages/spikes?

In this study, we employed morphologically realistic neuronal models in different configurations to address these questions about extracellular signatures of chemical synaptic *vs*. gap junctional inputs impinging on active or passive structures. Our analyses unveiled striking differences in polarities, spatiotemporal patterns, spectral signatures, and intracellular voltage relationships of extracellular potentials associated with inputs impinging on active dendrites through chemical synapses *vs*. gap junctions. We found these differences to be mediated by the differential dominance of receptor *vs*. active transmembrane currents associated with chemical synaptic *vs*. gap junctional inputs, respectively. The key distinctions in extracellular signatures of gap junctional inputs onto active structures emphasize the inadequacies associated with analyses that account solely for chemical synapses, strongly warranting the need to account for gap junctions in the analyses of extracellular potentials.

RESULTS

Synchronous inputs: Contrasting patterns of extracellular signatures associated with active dendritic chemical synapses *vs*. gap junctions.

First, we assessed the impact of synchronous excitatory inputs impinging on active or passive basal dendrites, either through chemical synapses or gap junctions, on extracellular potentials. To do this, several synapses or junctions that were randomly placed at different locations along the dendritic tree were synchronously activated. Intracellularly, these synchronous inputs yielded a somatic action potential irrespective of whether they arrived through chemical synapses or gap junctions. In striking contrast, extracellular signatures manifested a strong dependence on whether these synchronous inputs arrived through chemical synapses (Fig. 1*A*) or gap junctions (Fig. 1*B*). Specifically, the extracellular potential manifested as a sink (a negative deflection) at proximal and distal basal locations with synchronous excitatory chemical synapses (Fig. 1*A*). However, when synchronous gap junctional connectivity provided the excitatory inputs, extracellular potentials manifested a source (a positive deflection) at proximal and distal basal locations (Fig. 1*B*). The amplitudes of extracellular potentials, across all electrode locations spanning the basal tree, were comparable for analyses with active or passive dendrites (with the soma remaining active for either scenario) when synchronous stimulation arrived through chemical synapses (Fig. 1*C*). Remarkably however, the amplitudes of extracellular potentials showed significant reductions between active and passive cases, across all electrode locations spanning the basal tree, when synchronous inputs arrived through gap junctions (Fig. 1*D*). These observations held even when the number of synaptic or junctional contacts were reduced (Supplementary Fig. S2), and together point to dominant contributions of transmembrane currents from active dendrites to extracellular field potentials associated with synchronous gap junctional inputs (Fig. 1*D*). The striking reduction in the amplitudes, spanning orders of magnitude, of extracellular potentials with passive dendrites (Fig. 1*D*) explains why gap junctional contributions to LFPs have been historically neglected.

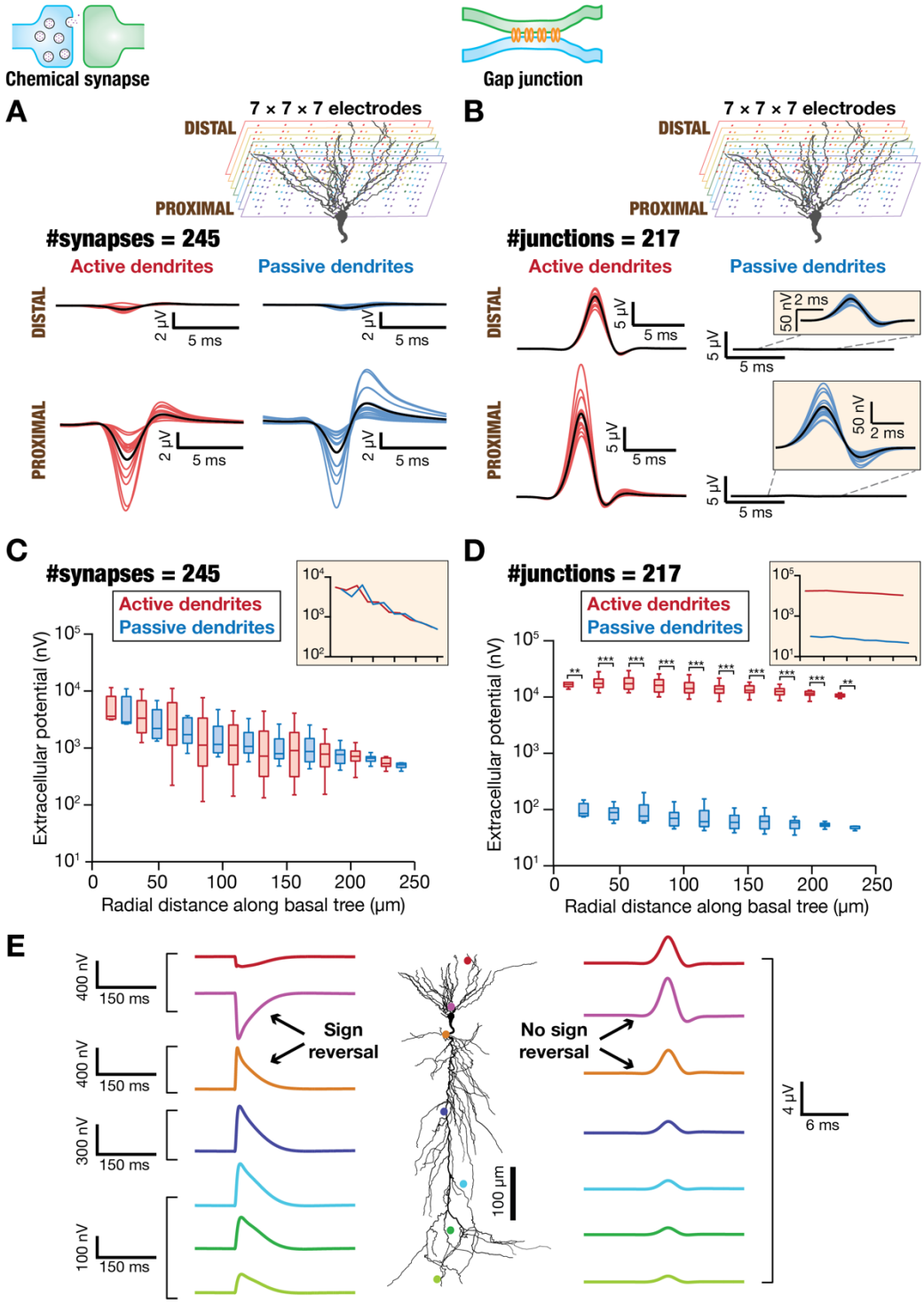

Figure 1. Contrasting extracellular signatures associated with active dendritic chemical synapses *vs.* gap junctions receiving synchronous inputs. ***A.*** *Top,* 3D electrode setup representing 7×7×7 (343 in total) electrode array spanning the basal dendrites of a CA1 pyramidal neuron morphology. Although the entire morphology was used for simulations spanning the apical and basal dendrites, the depiction here is restricted to the basal dendrites to emphasize electrode locations. *Bottom*, field potential traces from electrodes at proximal (15 traces representing different locations within 50–100 μm) and distal (21 traces representing different locations within 190–300 μm) locations along the somato-basal axis, when dendrites were active (*left*) or passive (*right*). Black traces depict the respective average trace across all distal or proximal locations. The 245 chemical synapses ($N_{syn} = 245$) which were randomly dispersed across the basal dendrites received synchronous inputs. ***B.*** Same as ***A***, but for external inputs arriving through gap junctions. The number of gap junctions $N_{jun} = 217$. ***C.*** Amplitudes of negative deflection of field potentials for all 343 electrodes, plotted as functions of radial distance of the electrode from the soma, for active and passive dendritic models receiving

synchronous inputs through chemical synapses ($N_{\text{syn}} = 245$). Inset shows plot of median field potential amplitude values as a function of distance for both active and passive dendritic configurations. ***D.*** Same as ***C***, but amplitudes of positive deflections in extracellular potentials associated with inputs arriving through gap junctions. The number of gap junctions $N_{\text{jun}} = 217$. Comparison of active *vs*. passive dendritic configurations in (***C–D***): * $p<0.05$, ** $p<0.01$, *** $p<0.001$, Wilcoxon rank-sum test. ***E.*** Extracellular electrodes were placed across the entire span of the neuron (active dendrites with no sodium) instead of being confined to the basal dendritic span (panels ***A–D***), with all parameters set identical to panels ***A–D***. A flip in the sign of the extracellular potentials may be noted for synchronous stimulation with chemical synapses (*Left*), but not with stimulation with gap junctions (*Right*).

To assess the spatial profile of the extracellular potentials with synchronous stimulus configurations, we extended the placement of extracellular electrodes beyond the basal dendritic span to cover the apical dendrites of the morphology. When synchronous inputs arrived through chemical synapses, we found an expected shift in the sign of deflection in the extracellular potentials on the apical side of the dendritic morphology (which received no synaptic inputs) (Fig. 1*E*) indicative of a sink-source dipole. In contrast, when synchronous inputs arrived through gap junctions, the deflection in the extracellular potentials stayed positive across the entire stretch of the morphology (Fig. 1*E*). The magnitude of deflections showed expected reductions with increasing distance from the basal dendrites, irrespective whether inputs arrived onto basal dendrites through chemical synapses or gap junctions (Fig. 1*E*).

Together, these observations unveiled crucial distinctions in the polarity and the spatiotemporal patterns of extracellular potentials associated with synchronous inputs impinging on active dendrites through chemical synapses *vs*. gap junctions. Importantly, these results also pointed to the dominant role of contributions from active dendritic transmembrane currents in shaping extracellular field potentials associated with gap junctional inputs.

Synchronous inputs: Outward transmembrane currents from active dendrites contribute to positive deflection in extracellular potentials associated with gap junctional inputs.

Which of the several transmembrane currents contributed to the striking differences in the profiles of extracellular potentials associated with chemical synapses *vs*. gap junctions? In systematically addressing this question, we repeated our experiments with synchronous stimuli with models where specific currents were turned off. We assessed extracellular potentials in models without sodium and/or leak potassium currents and compared the outcomes with the default active dendritic model outcomes (Fig. 2). With synchronous inputs arriving through chemical synapses, these analyses revealed a role for sodium currents and action potential generation in determining the biphasic nature of the deflections in the extracellular potentials around basal dendritic regions (Fig. 2*A*). In the absence of sodium channels, extracellular potentials at all basal dendritic locations showed negative deflections, reflecting the kinetics of inward synaptic currents, with significantly reduced

amplitudes (Fig. 2*A*). However, removal of leak currents did not yield pronounced changes in the extracellular potentials associated with synchronous inputs through chemical synapses (Fig. 2*A–B*). Along the basal dendritic neuropil, the values of peak negative deflection (Fig. 2*C*) and peak positive deflection (Fig. 2*D*) in the extracellular potentials reduced with electrode distance from the soma. The spatial profiles of deflections showed pronounced differences when sodium channels were removed but showed negligible differences with the removal of leak channels (Fig. 2*C–E*).

In contrast, in models that received synchronous inputs through gap junctions, both sodium channels and leak channels played crucial roles in shaping the spatiotemporal profile of extracellular potentials (Fig. 2*F–J*). First, deleting sodium channels from the models prominently suppressed both negative and positive deflections in the extracellular potentials (Fig. 2*F*, Fig. 2*H–I*). Second, and in striking contrast with models activated by chemical synapses (Fig. 2*A–E*), deletion of leak channels enhanced the negative peak but reduced the positive peak of extracellular potentials when sodium channels were intact (Fig. 2*F–I*). Finally, when both sodium channels and leak channels were removed, the kinetics (Fig. 2*F*) and spatial profiles of deflections in extracellular potentials (Fig. 2*H–J*) were comparable to those where only sodium channels were removed.

These observations point to a critical role for a competition between the outward leak currents and the inward sodium currents in defining the spatiotemporal profile of extracellular potentials associated with synchronous inputs arriving through gap junctions. To elaborate, excitatory gap junctional inputs triggered depolarizing voltage responses in the postsynaptic neuron, which translated to outward currents through the leak and the other active channels. When this depolarization crossed action potential threshold, an action potential was generated by the confluence of inward sodium currents followed by outward currents through the potassium channels. Therefore, the outward transmembrane currents triggered by gap junctional inputs preceded the inward sodium current that generated the action potentials, resulting in a scenario where the positive peak in the extracellular potential preceded the negative peak (Fig. 2*F–G*).

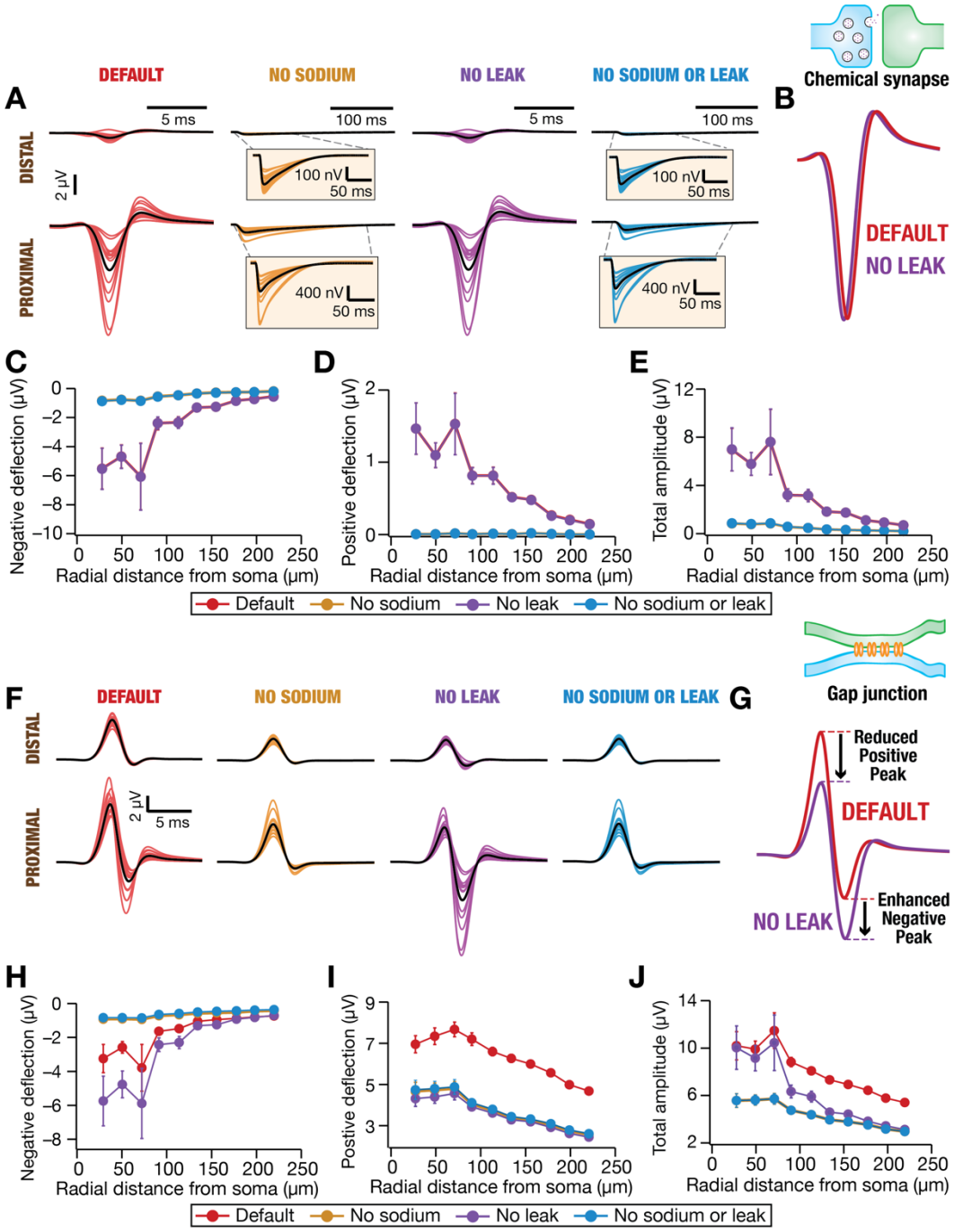

Figure 2. **Differential polarity of field potentials associated with synchronous inputs through chemical synapses *vs.* dendro-dendritic gap junctions on active dendrites.** ***A.*** Extracellular potentials from electrodes at proximal (15 colored traces represent different locations within 50–100 µm) and distal (21 colored traces represent different locations within 190–300 µm) locations along the somato-basal axis. Shown are traces for default (where all components were present), no sodium, no leak, and no sodium or leak scenarios for active dendritic structures. Black traces in each scenario depict the respective average trace across all distal or proximal locations. The 245 chemical synapses ($N_{\text{syn}} = 245$) which were randomly dispersed across the basal dendrites received synchronous inputs. ***B.*** Zoomed example trace (from a proximal electrode at 54 µm from soma) showing the impact of leak channels in shaping the extracellular potentials associated with active dendritic structures with (Default) and without leak channels (No leak). ***C–E.*** Mean and SEM of the amplitudes of negative deflection ***(C)***, positive deflection ***(D)***, and the total peak to peak amplitude ***(E)*** of the extracellular potentials, plotted as functions of radial distance of electrode location, for default, no sodium, no leak, and no sodium or leak scenarios for active dendritic structures. ***F–J.*** Same as panels ***A–E***, but for active dendritic structures receiving synchronous inputs through dendro-dendritic gap junctions ($N_{\text{jun}} = 99$).

When the sodium channels were deleted, the inward sodium current was suppressed and translated to a pronounced reductions in the negative (Fig. 2*H*) and the positive deflections (Fig. 2*I*) in the extracellular potentials (associated with gap junctional inputs). On the other hand, when leak channels were deleted, the outward leak current generated by gap-junctional depolarization and by the action potential were reduced (Fig. 2*F–G*). Together, such a scenario resulted in a reduced positive peak and an enhanced negative peak in the absence of leak channels but in the presence of sodium channels (Fig. 2*F–I*). Sodium channels were essential because they amplify gap junctional voltage depolarizations and mediate action potential generation. When sodium channels were absent, the outward currents triggered by gap-junctional depolarization dominated the extracellular potentials, with leak currents playing a minimal role in shaping extracellular potentials (compare "no sodium" *vs.* "no sodium or leak" cases in Fig. 2*F–J*).

What were the contributions of the different transmembrane currents to the extracellular potentials across the different scenarios presented above? We plotted the intracellular voltages and all transmembrane currents as functions of distance for each configuration assessed (Fig. 3). As expected, the presence of sodium channels yielded an action potential, irrespective of whether synchronous inputs came through chemical synapses (Fig. 3*A*) or through gap junctions (Fig. 3*C*). The presence of an action potential translated to large driving forces for all ionic currents, including currents through synaptic receptors (Fig. 3*A–B*, Fig. 3*D*). In addition, the large temporal derivate associated with action potentials also translated to higher values of capacitive current in the presence of sodium channels (Fig. 3*B*, Fig. 3*D*). The higher leak currents in the presence of sodium channels (Fig. 3*B*, Fig. 3*D*) contributed to the shifts in negative and positive peaks in extracellular potentials that were triggered by deletion of leak channels (Fig. 2*F–J*).

An important observation here is related to the current through HCN channels in the presence of abrupt large-amplitude voltage deflections, such as those observed with synchronous synaptic input. We noted that except for one case ("No sodium or leak" with chemical synapses), all average HCN current values were positive in sign (Fig. 3*B*, Fig. 3*D*). How do HCN channels, which typically carry inward transmembrane currents that are negative in sign, yield positive outward currents? HCN channels are active at rest and are endowed with slow activation/deactivation kinetics with a time constant ranging from tens to hundreds of milliseconds (Robinson and Siegelbaum, 2003; Biel et al., 2009; Shah, 2014; Combe and Gasparini, 2021; Mishra and Narayanan, 2023). With synchronous inputs impinging on the neuron, the transition from rest to large depolarization (which trigger action potentials in the presence of sodium channels) is fast. The fast kinetics of the depolarization implies that the active fraction of slow HCN channels does not have sufficient time for deactivation. Thus, once the membrane voltage crosses

the reversal potential of HCN channels ($E_h = -30$ mV), HCN current ($I_h = g_{\mathrm{HCN}}(V - E_h)$) becomes positive as the driving force ($V - E_h$) becomes positive and the resting conductance remains non-zero. Together, in scenarios where the depolarizing voltage kinetics is faster than the deactivation kinetics of HCN channels towards crossing E_h, HCN channels yield an outward current (Supplementary Fig. S3). It is important to note that these outward currents through HCN channels (Fig. 3) also contribute to the positive deflections in extracellular potentials observed under different conditions (Fig. 2).

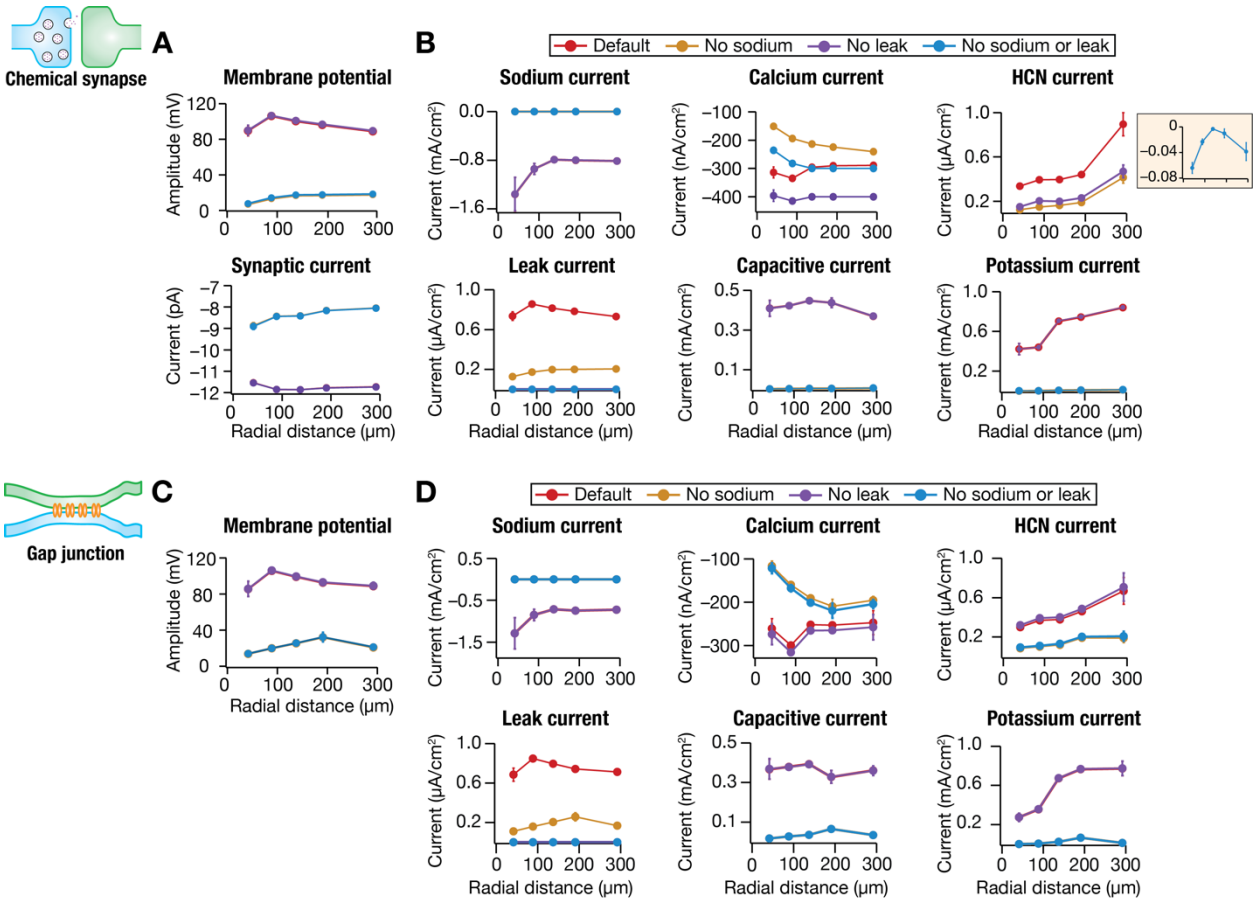

Figure 3. **Ionic basis of the differential contributions of transmembrane currents to field potentials associated with synchronous inputs arriving through chemical synapses *vs.* gap junctions on active dendrites. *A*.** Mean and SEM of peak membrane voltages (*top*) and peak synaptic currents (*bottom*) from across somato-basal locations recorded intracellularly for all 4 model configurations. The 4 different model configurations shown are the default active model, and the active models where sodium channels, leak channels, or both sodium and leak channels were absent. It may be noted that there were no action potentials or dendritic spikes when there were no sodium channels in the models. The dependence of synaptic current on the membrane potential, acting as the driving force, may also be noted. ***B***. Mean and SEM of peak values of transmembrane sodium, calcium (*T*-type, *L*-type, *R*-type, and *N*-type), HCN, leak, capacitive, and potassium (*A*-type, delayed rectifier, and *M*-type) currents for different active models receiving synchronous inputs through chemical synapses, plotted as functions of radial distance from soma for all 4 model configurations. ***C–D***. Same as panels *A–B*, but with different configurations of active models receiving synchronous inputs through gap junctions. There are no synaptic currents plotted here as there are no transmembrane synaptic currents associated with gap junctions.

Together, our results unveil stark differences in the extracellular field potentials associated with synchronous inputs, depending on whether such inputs arrived onto active dendrites through chemical synapses or gap junctions. Whereas leak channels played minimal roles in shaping extracellular potentials when inputs arrived through chemical synapses, they played a prominent role in defining extracellular potentials when inputs arrived through gap junctions. Our results showed that the striking polarity differences observed in extracellular potentials associated with chemical synapses *vs*. gap junctions (Fig. 1*A–B*) were driven by two prominent factors: (i) the absence of inward transmembrane currents with gap junctional inputs; and (ii) the presence of outward currents (through leak, potassium, and HCN channels) associated with gap-junctional depolarization and action potentials triggered by such depolarization (Figs. 2–3).

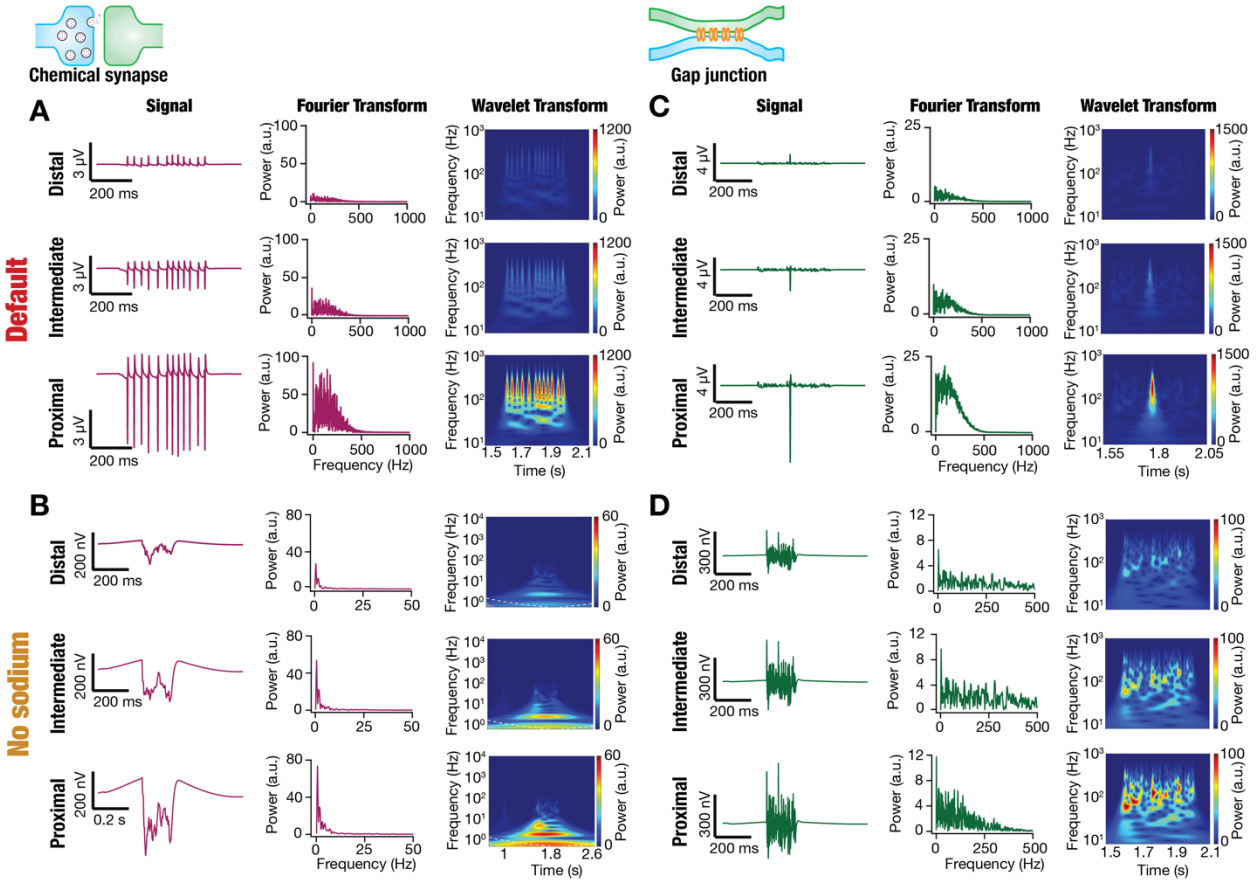

Figure 4. **Differential spatiotemporal structure of field potentials associated with active dendrites receiving low-frequency random inputs through chemical synapses *vs.* gap junctions.** ***A***. Distance-wise LFP responses to low-frequency random inputs (LFRI) impinging on active dendrites through chemical synapses. *Rows 1–3:* LFP data from electrodes located at a distal (~152 μm; *Row 1*), intermediate (~97 μm; *Row 2*), and proximal (~55 μm) locations with reference to their radial distance from the soma. *Column 1:* time-domain signal. *Column 2:* Fourier transform of the signal shown in *Column 1*. *Column 3:* spectrogram of the signal shown in *Column 1* computed using wavelet transform. ***B***. Same as panel (***A***) but for active model lacking sodium conductance. ***C–D***. Same as panels (***A–B***), except low-frequency random inputs impinged onto active dendrites through gap junctions.

Random inputs: Dichotomy in extracellular potentials associated with asynchronous inputs through chemical synapses *vs*. gap junctions.

We next explored if there were distinctions between extracellular potentials stemming from random inputs through chemical *vs.* electrical synapses. We computed extracellular potentials from models receiving low- (Fig. 4) and high-frequency (Supplementary Fig. S4) random inputs (LFRI and HFRI) onto active dendrites through chemical synapses or gap junctions. For both LFRI and HFRI, the power associated with extracellular potentials was higher when asynchronous inputs arrived through chemical synapses compared to their arrival through gap junctions (Fig. 4; Supplementary Fig. S4). These observations held irrespective of whether models were endowed with sodium channels or not (Fig. 4; Supplementary Fig. S4). Across scenarios, the power associated with extracellular potentials reduced with increasing distance from the cell body (Fig. 4; Supplementary Fig. S4). We attributed these differences to the presence of an additional transmembrane current through the synaptic receptors, in models that received inputs through chemical synapses when compared to models receiving inputs through gap junctions. Importantly, the presence of the large inward synaptic currents in structures receiving chemical synaptic inputs also translated to predominantly negative deflections in associated extracellular potentials. In comparison, extracellular potentials associated with models that received gap junctional inputs showed deflections on both positive and negative directions. This distinction in the sign of the extracellular potentials associated with chemical synapses *vs*. gap junctions was prominently visible in models where there were no sodium channels (Fig. 4; Supplementary Fig. S4). Together, these results revealed distinctions in extracellular potentials associated with active dendritic structures receiving random inputs at different frequencies through chemical synapses *vs*. gap junctions.

Rhythmic oscillatory inputs: Distinctions in spectral characteristics of extracellular potentials associated with chemical synapses *vs*. gap junctions on active dendrites.

In a third set of experiments, we activated the chemical synapses or the gaps junctions with rhythmic inputs at different physiologically relevant frequencies (Fig. 5). We computed the associated extracellular potentials and studied their spectral properties in models that were endowed with active or passive dendrites (Fig. 5). As expected, the extracellular potentials manifested oscillatory patterns in the same range as that of the stimulation frequencies, irrespective of whether the inputs came through chemical synapses or gap junctions and irrespective of whether the dendrites were active or passive. We computed the peak power from the Fourier spectra of extracellular potentials from all 343 electrodes for each scenario, involving different frequencies (spanning 1–128 Hz in

octaves), model configurations (active *vs*. passive dendrites), and modes of stimulation (through chemical synapses *vs*. gap junctions) (Fig. 6).

As with other stimulus configurations before, the presence of an additional transmembrane current with chemical synaptic stimulation contributed to differences in extracellular potentials associated with chemical synapses and gap junctions. First, these differences implied that there were dominant contributions from active dendritic transmembrane currents to extracellular field potentials associated with gap junctional inputs (Fig. 6*B*), but not with chemical synaptic inputs (Fig. 6*A*). This was inferred from the pronounced differences observed in active *vs*. passive model configurations with gap junction inputs (Fig. 6*B*), but not with chemical synaptic inputs (Fig. 6*A*; except for 128 Hz where pronounced differences were noted for both chemical synapses and gap junctions). Specifically, across frequencies, the LFP power with active dendrites was larger than LFP power with passive dendrites when inputs impinged through gap junctions (Fig. 6*B*), implying a significant contribution from active dendritic transmembrane currents.

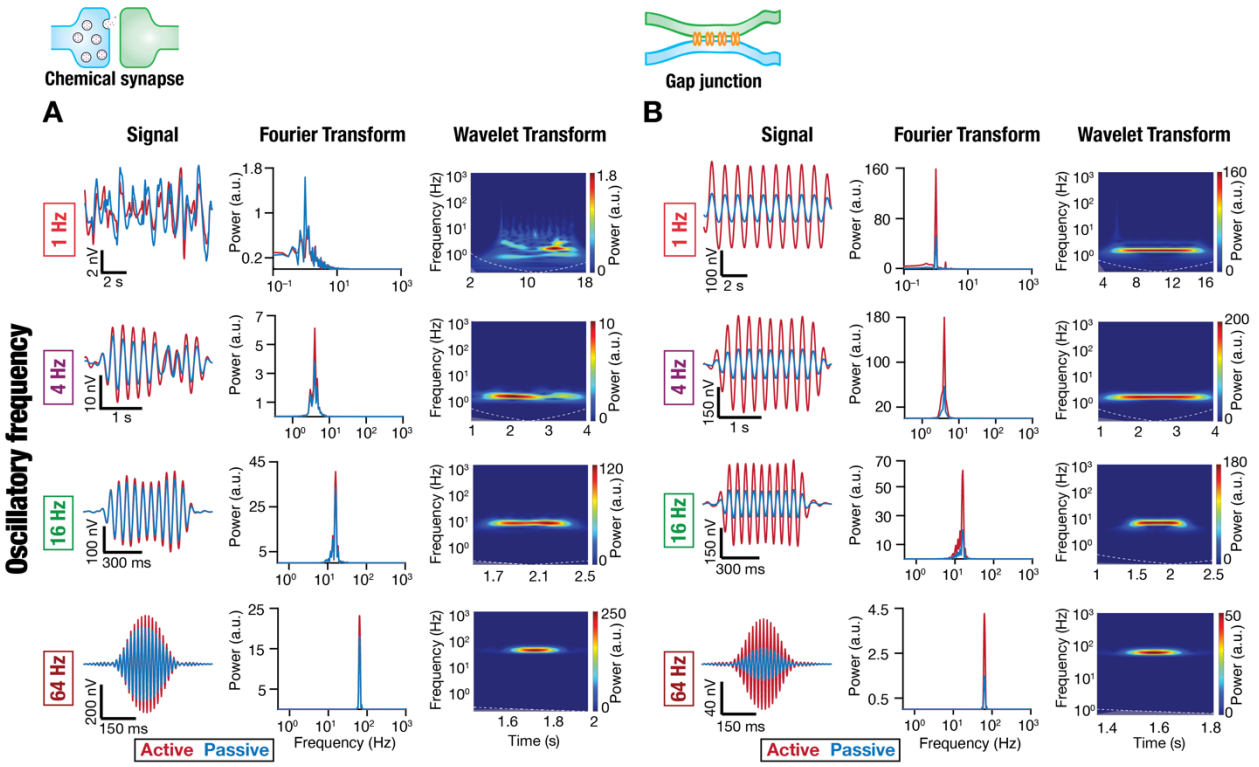

Figure 5. Dominance of specific oscillatory bands in field potentials depended on whether inputs onto active dendrites were received through chemical synapses or gap junctions. ***A***. Example LFP responses to rhythmic inputs at different (1–64 Hz) frequencies and their spectral signatures, shown for simulations performed with active or passive basal dendrites receiving rhythmic inputs through chemical synapses. Each row shows the filtered LFP signal at an electrode placed ~97 µm from the soma, the Fourier power spectrum, and the wavelet spectrogram for the LFP signal. Different rows depict different input frequency values for the rhythmic input (1 Hz, 4 Hz, 16 Hz, and 64 Hz). ***B***. Same as *(A)* but for the rhythmic inputs impinging on basal dendrites at different frequencies through gap junctions. All simulations depicted here were performed in the absence of sodium channels to avoid spiking.

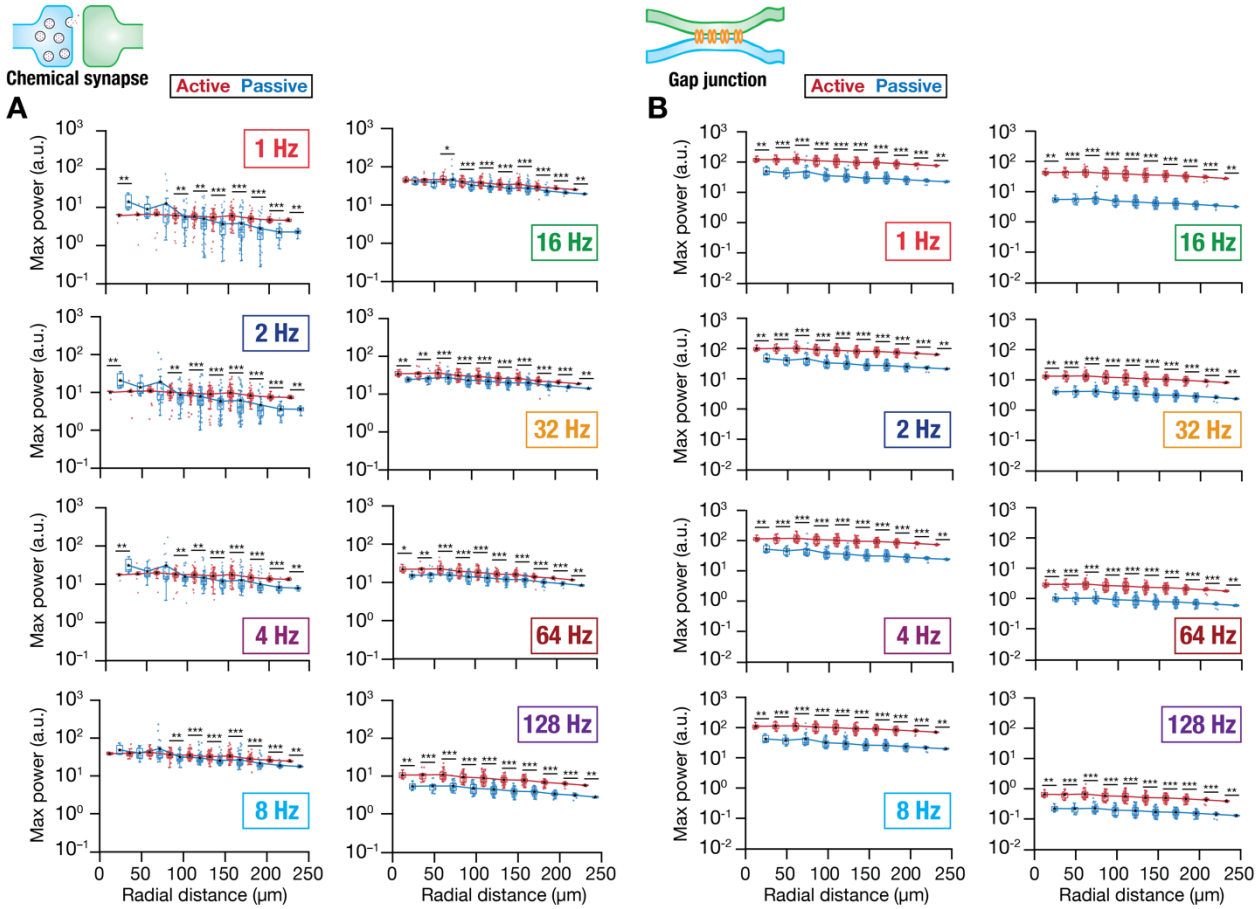

Figure 6. Distance-dependence of spectral power in specific bands of field potentials associated with active dendrites receiving rhythmic inputs through chemical synapses or gap junctions. ***A***. Maximum power in LFP responses associated with rhythmic inputs at different (1–128 Hz) frequencies, shown for simulations performed with active or passive basal dendrites receiving these rhythmic inputs through chemical synapses. All electrodes at specific radial distances are depicted for each scenario. The frequency of the rhythmic input is highlighted in each panel. ***B***. Same as *(**A**)* but for the rhythmic inputs impinging on basal dendrites at different frequencies through gap junctions. Across all plots, lines connect the respective median values (represented by black stars). All simulations depicted here were performed in the absence of sodium channels to avoid spiking. * $p<0.05$, ** $p<0.01$, *** $p<0.001$ (Wilcoxon rank-sum test)

Second, the dominant role of the receptor currents with chemical synaptic stimulation implied that there was a strong transmembrane component spanning all frequencies. Thus, we observed relatively higher power even at higher frequencies (say, for 64 Hz or 128 Hz) in the extracellular potentials (as well as total transmembrane currents) with chemical synaptic stimulation (Fig. 7*A–B*) compared to those with gap junctional stimulation (Fig. 7*C–D*). With gap junctional rhythmic inputs, the power of extracellular potentials (and total transmembrane currents) at higher frequencies was low (Fig. 7*C–D*), owing to their origins being entirely through transmembrane currents driven by a membrane-filtered voltage waveform. Specifically, as the membrane resistor-capacitor circuit acts to suppress higher frequencies, intracellular voltage responses to high-frequency current inputs were lower in amplitude yielding low-amplitude transmembrane currents due to low driving forces. Although such filtering is common to both chemical synaptic and gap

junctional inputs, the reliance of LFP associated with gap junctional inputs on voltage-driven transmembrane currents translate to the distinctions observed in extracellular signatures associated with chemical synapses (Fig. 7*A–B*) *vs*. gap junctions (Fig. 7*C–D*).

Third, the differences in the contributions of active transmembrane currents *vs*. receptor currents to the LFP also translated to a differential emphasis of frequencies associated with gap junctions *vs*. chemical synaptic stimulations (Fig. 7*A–D*). Specifically, rhythmic inputs at 8 Hz and 16 Hz showed maximal power in the extracellular potentials associated with chemical synapses, irrespective of whether the dendrites were active or passive (Fig. 7*A–B*). On the other hand, with gap junctional rhythmic stimulation, we found that extracellular potentials associated with lower frequencies (1–8 Hz) manifested much higher power compared to the higher frequencies, again irrespective of whether the dendrites were active or passive (Fig. 7*C–D*). Importantly, there was minimal reduction in power of extracellular potentials across most frequencies (except at 128 Hz) between active (Fig. 6*A*, Fig. 7*A*) and passive (Fig. 6*A*, Fig. 7*B*) dendritic configurations with chemical synaptic stimulation. In striking contrast, there was a large reduction in power when active components were removed from the dendrites as rhythmic inputs arrived through gap junctions (Fig. 6*B*, Fig. 7*C* vs. Fig. 7*D*). These observations reaffirm the relative dominance of receptor currents and active transmembrane currents for chemical synaptic and gap junctional stimulus conditions, respectively.

Fourth, we looked at phase differences in extracellular potentials across the neuronal morphology to span apical dendrites as well (Supplementary Fig. S5). We found important differences in the spatiotemporal profiles of extracellular potentials obtained with rhythmic inputs arriving through chemical synapses *vs*. gap junctions. With active dendritic structures, we found a progressive shift in the phase of extracellular potentials as the electrode location moved away from the basal dendrites where the chemical synaptic inputs were impinging (Supplementary Fig. S5*A*). However, there was negligible phase difference across electrode locations when inputs onto basal dendrites arrived through gap junctions (Supplementary Fig. S5*A*). With passive dendritic structures, a similar relative shift in phase was observed between chemical synaptic *vs*. gap junctional inputs. However, a smaller phase shift was observed across electrodes when oscillatory inputs arrived through gap junctions (Supplementary Fig. S5*B*).

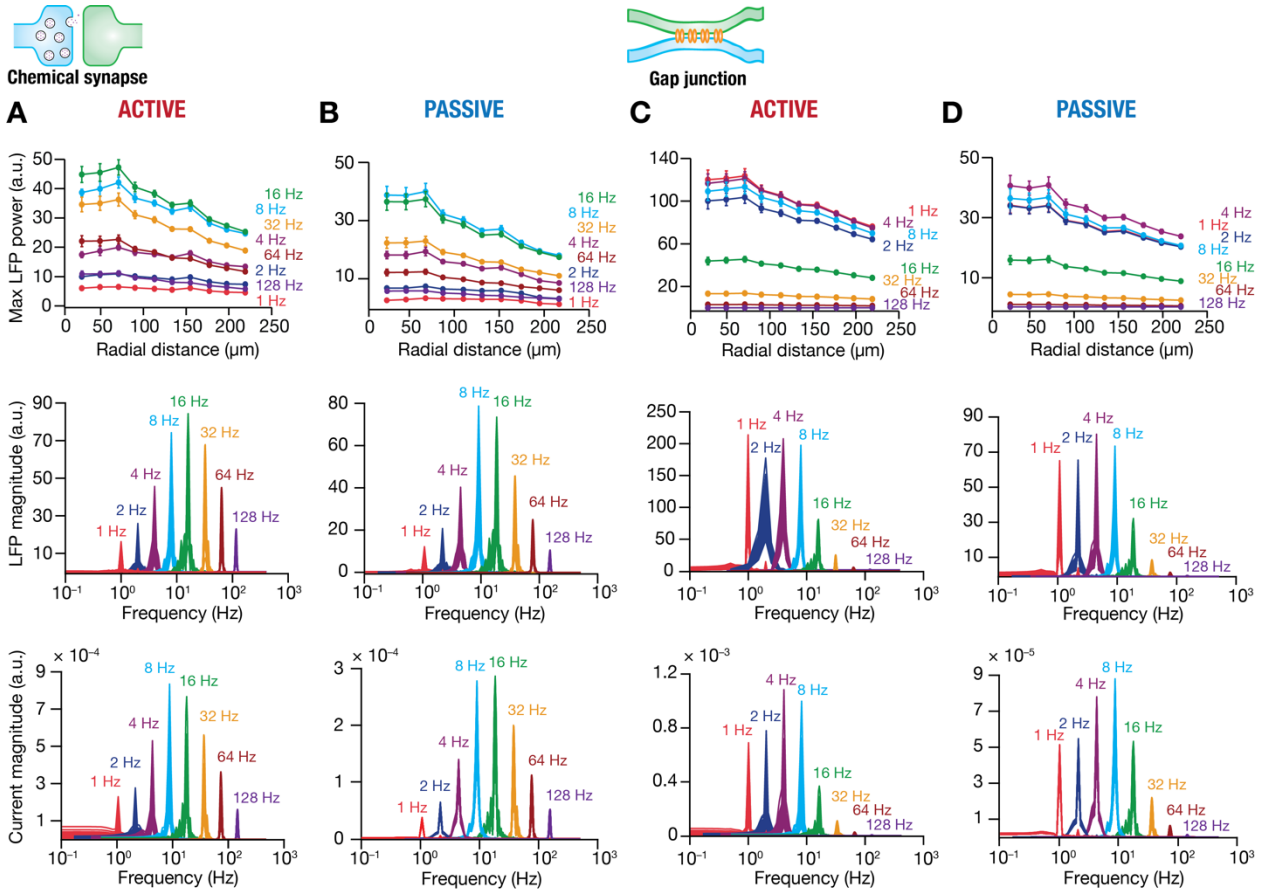

Figure 7. Transmembrane currents driven by voltage responses mediate the differential emphasis of specific oscillatory bands in field potentials associated with chemical synapses *vs.* gap junctions on active dendrites. ***A.*** *Row 1:* Distance-dependent maximal power of local field potentials recorded at different electrodes (shown as mean and SEM) associated with neuronal response to rhythmic inputs at different frequencies impinging on the active basal dendritic model through chemical synapses. *Row 2:* Fourier power spectra for all field potentials at different frequencies of the rhythmic inputs. Each trace for a given frequency represents different electrodes. *Row 3:* Fourier spectra of the filtered total transmembrane current for each frequency of rhythmic inputs, from each basal dendritic compartment. ***B.*** Same as panel ***A***, but for simulations performed with passive dendrites. ***C–D.*** Same as *(**A–B**)*, but with rhythmic inputs coming through gap junctions. All simulations depicted here were performed in the absence of sodium channels to avoid spiking.

Together, we observed several crucial distinctions in the spectral characteristics of extracellular potentials associated with gap junctional *vs*. chemical synaptic rhythmic inputs impinging on active dendrites. We found these distinctions to be attributable to the relative contributions of receptor *vs*. active transmembrane currents to extracellular potentials associated with chemical synaptic *vs*. gap junctional inputs.

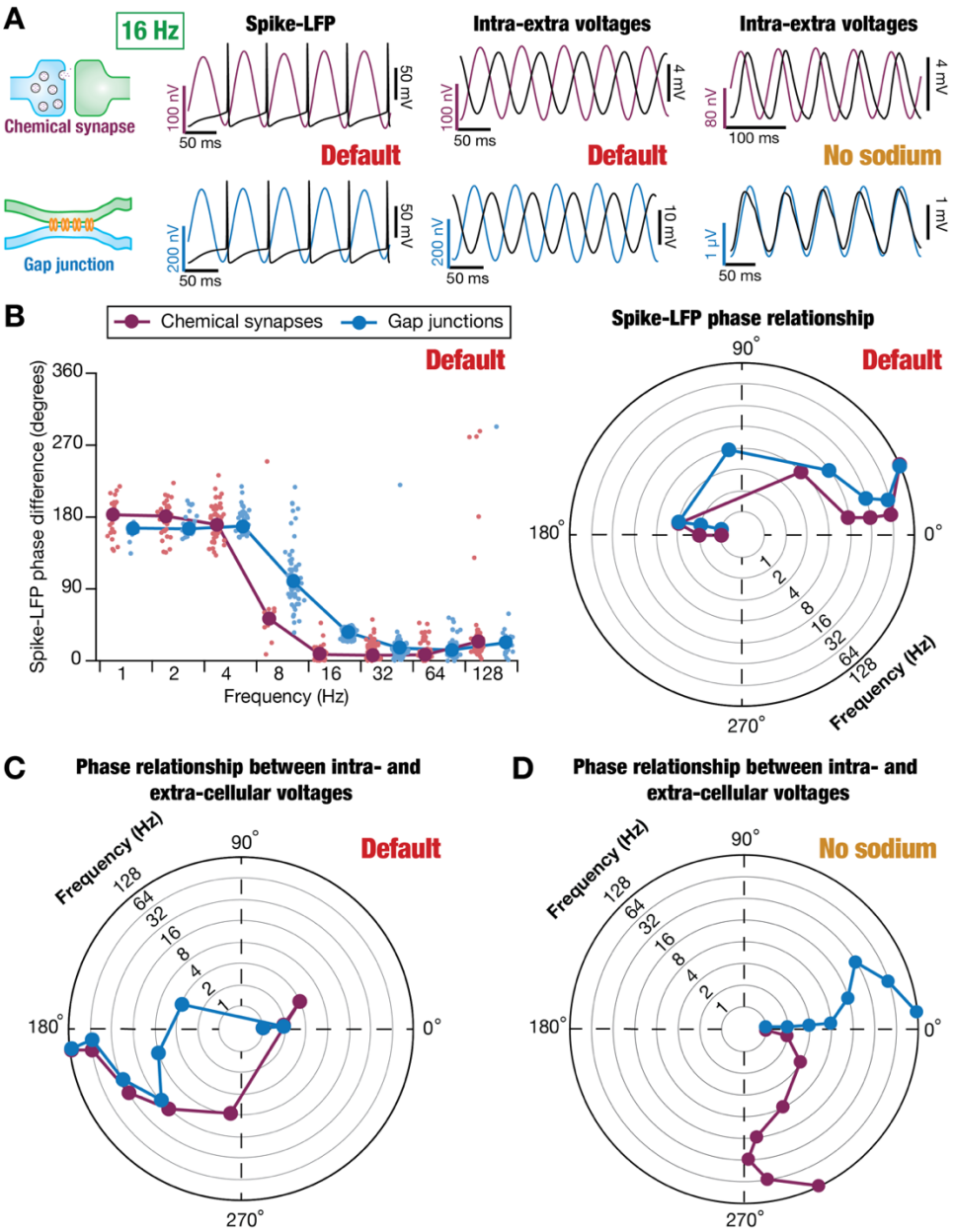

Figure 8. Differential phase relationship between local field potentials and spikes associated with rhythmic inputs through chemical synapses *vs.* gap junctions on active dendrites. *A.* Example LFP traces (color coded based on whether they are associated with chemical synapses in dark pink or gap junctions in blue) and simultaneously recorded intracellular somatic voltage traces (Black) for neurons receiving rhythmic inputs through chemical synapses (*top*) or gap junctions (*bottom*). Shown are traces with default model configuration where all channels were intact (*left*), traces where the intracellular traces were filtered to the respective band (*middle*), and extracellular/intracellular traces obtained in the absence of sodium channels (*right*). ***B.*** *Left,* Spike phase with reference to local field potentials for each spike (lighter circles) for oscillatory inputs at different frequencies impinging on active dendrites through chemical synapses *vs.* gap junctions. Dark-colored circles represent the median values at each frequency for the respective group. *Right,* Polar version of the plot showing median of spike-LFP phases over five trials for rhythmic inputs at different frequencies through chemical synapses and gap junctions. The different frequencies are represented along the concentric circles and the corresponding spike-LFP phase values are plotted along the angular axis. ***C.*** Polar plot with median of phases obtained from cross-correlation of *filtered* intracellular potential and corresponding LFP traces at respective frequencies over all trials. These plots were derived from the same intracellular traces as in panel *A* but represent phase differences between extracellular traces and the entire filtered intracellular voltage trace. ***D.*** Polar plot of phases obtained from cross-correlation between intracellular potential (without sodium conductance) and corresponding LFP traces when oscillatory inputs were presented through chemical synapses or gap junctions.

Rhythmic oscillatory inputs: LFP-spike phase relationship relied on the oscillatory frequency and on whether inputs arrived through chemical synapses or gap junctions.

The phase of spikes in individual neurons with reference to extracellular potentials are studied in phase coding schemas and in assessing synchrony. Given key differences in the extracellular spectral signatures (Figs. 5–7) and spatiotemporal profiles of LFPs (Supplementary Fig. S5), we asked if there were differences in the phase relationship between spikes and extracellular potentials when rhythmic inputs arrived through chemical synapses *vs*. gap junctions (Fig. 8; Supplementary Figs. S6–S11). We used extracellular potentials from a soma-proximal electrode as reference and computed phase of somatic action potentials, considering trough of the LFP trace as zero degrees. These experiments and analyses were repeated across different trials (which were different in terms of synaptic localization profiles), each spanning multiple cycles, with rhythmic inputs arriving at different frequencies through chemical synapses or gap junctions onto different model configurations (Fig. 8; Supplementary Figs. S6–S11). Across frequencies and irrespective of whether inputs arrived through chemical synapses or gap junctions, spikes manifested phase locking to LFP oscillations (Fig. 8*A–B*; Supplementary Figs. S6–S7). There were frequency-dependent differences in spike phases, depending on whether rhythmic inputs arrived through chemical synapses or gap junctions (Fig. 8*A–B*; Supplementary Figs. S6–S7). Irrespective of whether inputs arrived through chemical synapses or gap junctions, the median spike phase (across trials and cycles) progressively shifted from ~180° to ~0° with increase in frequency from 1 Hz to 128 Hz (Fig. 8*B*). However, for intermediate frequency values (8 Hz, 16 Hz), there were large differences in the spike phase values for models receiving inputs through chemical synapses *vs*. gap junctions.

To understand these spike phase profiles across frequencies and across type of synapses, we compared the phase difference between intracellular somatic voltage waveforms and peri-somatic extracellular potentials. We filtered the waveforms with reference to the specific frequency of rhythmic inputs they were obtained in response with (Supplementary Table S3) and performed cross-correlation analysis to compute phase differences between intra- and extra-cellular potentials (Fig. 8*C*; Supplementary Figs. S8–S9). We repeated these analyses across different trials and phase differences were plotted. Consistent with what we observed with spike phases earlier, we found that the phase difference between extra- and intra-cellular potentials progressively shifted from ~0° to ~180° as frequency increases. Note that a spike that occurs at the peak of the extracellular potential (with the trough designated as 0°) would be assigned a spike phase of 180°. Under this scenario, the peak of intracellular voltage would match with the peak of extracellular waveform, thereby translating to a 0° phase difference between intra- and extracellular voltages. We observed

negligible differences in this phase relationship for chemical synapses *vs*. gap junctions for low (1–2 Hz) and high frequencies (16–128 Hz). However, for intermediate frequency values (4–8 Hz), there were differences in the phase relationship between intra- and extra-cellular potentials depending on whether rhythmic inputs arrived through chemical synapses or gap junctions (Fig. 8*C*; Supplementary Figs. S8–S9).

Finally, to assess the specific contributions of the spike generation and sodium channels to these phase relationships, we repeated our cross-correlation analyses on simulations that were performed in the absence of sodium channels (Fig. 8*D*; Supplementary Figs. S10–S11). In this scenario, whereas the phase relationships between intra- and extra-cellular voltages were comparable for low frequencies (1–2 Hz), there was a dramatic deviation between phase plots obtained with chemical synaptic *vs*. gap junctional inputs (Fig. 8*D*; Supplementary Figs. S10–S11). Specifically, at higher frequencies (observed maximally at 16 Hz), the intracellular voltage waveform lagged the extracellular voltage with chemical synaptic rhythmic stimulation (Fig. 8*D*; Supplementary Figs. S10). In contrast, the intracellular waveform manifested a small lead with reference to the extracellular waveform with gap junctional rhythmic stimulation (Fig. 8*D*; Supplementary Figs. S11). In either case, the magnitude of lead or the lag never crossed 90° for any of the analyzed frequencies.

These observations point to a scenario where the depolarization induced by the receptor currents trigger the activation of outward currents, which dominate the extracellular potentials with chemical synaptic stimulation in the absence of sodium channels (Fig. 8*D*; Supplementary Figs. S10). The transmembrane inward receptor current and the outward currents together resulted in a phase lead in the LFP observed with chemical synaptic stimulation, especially with higher frequencies (Fig. 8*D*; Supplementary Figs. S10). On the other hand, with gap junctional stimulation, depolarization triggered by gap junctional currents result in net outward currents following the intracellular depolarization caused by the rhythmic inputs. Such a scenario translates to a lag in the extracellular voltage trace compared to its intracellular counterpart (Fig. 8*D*; Supplementary Figs. S11). In the presence of sodium channels, the large voltage deflections and spikes generated, the consequent increase in driving force, the inward transmembrane sodium current, the activation-inactivation profiles of all active channels, the spatiotemporal profile of stimulation, the membrane time constant, and the specific kinetics of the synaptic activation together result in a scenario where spike phases are variable for gap junctions *vs*. synaptic stimulation (for intermediate frequencies).

DISCUSSION

A diverse interplay involving several factors — such as neuronal morphology, organization of different morphologies and afferent inputs onto them, active components in different neuronal processes, spatiotemporal patterns of afferent inputs onto neurons, receptor localization and kinetics, intraneuronal filtering, neuropil properties, ephaptic coupling, interactions among cross-cellular transmembrane currents, and electrode localization — shapes extracellular potentials. Our analyses add a further layer of complexity by demonstrating stark differences in extracellular potentials associated with inputs arriving onto active dendrites through chemical synapses *vs*. gap junctions. Considering the crucial role of gap junctions in several networks across the brain, it is critical that LFP analyses and interpretations account for whether inputs arrive through gap junctions or through chemical synapses. Our analyses place strong emphasis on accounting for the distinct contributions of gap junctional inputs onto active structures (*e.g.*, neuronal dendritic and axonal compartments, neuronal and glial soma, glial processes) to extracellular field potentials. The absence of receptor transmembrane currents and the dominance of voltage-driven passive/active transmembrane currents in determining extracellular potentials associated with gap junctional inputs are crucial factors that must be accounted for in interpreting extracellular potentials. Our study emphasizes the need for quantitative assessment of how chemical and electrical synapses individually influence extracellular patterns across different brain regions and how their combined impact on extracellular potentials contribute to specific aspects of network physiology and accurate interpretations of brain signals.

Dominance of active dendritic currents with LFP associated with gap junctions.

When dendrites were thought to be passive, LFPs were considered to be predominantly reflective of currents through synaptic receptors that were present on different postsynaptic locations on neurons. However, it is now clear that dendrites are active in that they are endowed with several voltage- and/or calcium-gated ion channels. These dendritic active currents make predominant contributions to LFP apart from receptor currents. The receptor current, all active currents, the capacitive and leak currents across the neuronal morphology obey Kirchoff's current law (KCL), thus creating source-sink dipoles depending on the open or closed nature of the field organization (Buzsaki et al., 2012; Einevoll et al., 2013; Reimann et al., 2013; Sinha and Narayanan, 2015; Ness et al., 2016; Sinha and Narayanan, 2022; Halnes et al., 2024).

However, much of these analyses have been limited to scenarios where synaptic inputs are received exclusively through chemical synapses, which manifest a transmembrane current through the postsynaptic receptors. With electrical synapses, the KCL is balanced without a transmembrane synaptic current because gap junctional inputs are direct intracellular inputs into the neuron that do not manifest a direct transmembrane current. Therefore, with chemical synapses, the synaptic current provides an extracellular field component that precedes the voltage response to the synaptic current. The voltage deflection caused by chemical synaptic or gap junctional inputs would yield additional transmembrane currents in the form of the leak current, the capacitive current, and the active currents. These additional transmembrane currents from different neuronal locations summate at an electrode location weighted in distance-dependent manner to eventually yield the extracellular potential. While these voltage-response-induced currents are common to both chemical synapses and gap junctions, the absence of transmembrane synaptic currents with gap junctional inputs results in important and striking differences in the extracellular signatures associated with gap junctions and chemical synapses. If dendrites were passive, the only transmembrane current components associated with gap junctional inputs would have been the leak and the capacitive currents. But, in a scenario where dendrites are active, the extracellular field was defined by active transmembrane currents as well, together contributing to the notable distinctions reported here.

In the absence of transmembrane synaptic currents, the outward currents that were triggered by depolarization dominated the extracellular field potentials with synchronous synaptic inputs. There was a striking difference in polarity of the field potentials associated with chemical synapses and gap junctions. These differences resulted a scenario where there was no source-sink dipoles in extracellular potentials across the neuronal morphology because gap junctions imply that inputs were injected directly into the neuron. The shape of the extracellular potentials, their polarities, and their spatial distributions have all been typically understood from the perspective of synaptic potentials. Our study demonstrates that these analyses do not hold for active structures connected through gap junctions. These observations emphasize the need to revisit the frameworks for understanding field potentials, especially in brain regions where there are strong gap junctional connectivity across neurons (Traub, 1995; Bennett and Zukin, 2004; Connors and Long, 2004; Sohl et al., 2005; Traub et al., 2018), including scenarios where there is mixed connectivity involving gap junctions as well as chemical synapses (Hamzei-Sichani et al., 2012; Nagy et al., 2019).

High-frequency LFP power was suppressed with gap junctional inputs.

The absence of transmembrane receptor currents with gap junctional stimulation implies that membrane filtering has a dominant impact on extracellular potentials when synaptic inputs arrive through gap junctions. A direct consequence of such strong dependence on membrane filtering, which predominantly acts to suppress high frequencies, is that there is pronounced attenuation of extracellular potentials associated with high-frequency rhythmic inputs arriving through gap junctions (Figs. 5–7). Although high-frequency chemical synaptic inputs also face the same membrane filtering, the transmembrane receptor component provides an important additional contribution to extracellular potentials beyond the voltage-driven transmembrane currents.

There are several implications to this. First, although there might be strong high-frequency interactions between neurons coupled through gap junctions, the extracellular signatures associated with such strong interactions would be weak unless these interactions produce action potentials and translate to large extracellular signatures. Second, oscillatory networks in low frequency (say, delta or theta frequency ranges) connected through gap junctions might manifest strong extracellular signatures associated with rhythmic inputs. The strong dependence on membrane filtering implies that the extracellular potentials might not be of high amplitude if the oscillatory inputs through gap junctions were in the high-frequency ranges (say high-gamma or ripple band oscillations). Third, the extent of spatial spread of field potentials, especially in low frequencies, would strongly depend on gap junctional connectivity across active structures. Finally, the exact nature of frequency dependence would strongly rely on the kind of active conductances expressed by the different compartments across the neuron. Given that there are no transmembrane receptor currents associated with gap junctional inputs, there is the sole reliance of extracellular potentials on the voltage-driven transmembrane currents (leak, capacitive, and active currents). Therefore, it is essential that analyses and interpretation of extracellular potentials to oscillatory inputs of different frequencies account for not just the origins of synaptic inputs, but also the membrane composition of all neurons and their dendrites in a network-specific fashion. Generalization of any kind that does not account for the specific synapses, the specific frequencies involved, or the membrane composition (including ion channels, pumps, transporters) of all cells in the network are bound to yield incorrect conclusions.

Phase relationship between intracellular and extracellular potentials.

The phase relationship between the intracellular voltages and extracellular potentials are dependent on several factors. First, as the receptor currents are inward and the consequent intracellular voltage response is a depolarization, that constitutes a 180° phase shift given that the receptor currents dominantly contribute to extracellular potentials associated with chemical synapses. Second, the capacitive transmembrane current for a pure oscillatory voltage response is 90° given that the capacitive current is directly related to the derivative of the voltage. The capacitive component will increase in amplitude with increasing frequencies owing to the dependence on the derivative of the voltage. Third, the presence of low-pass RC filtering implies that the voltage response is higher for low frequencies and lower at high frequencies. These differences in voltage amplitudes translate to differences in voltage-gated active channel currents, driving force differences for all transmembrane ionic currents including receptor currents, and as differences in capacitive current.

Fourth, depending on the slow and fast kinetics of the ion channels and the frequency at which the stimulation is presented, certain channel currents will be in phase with the voltage (*e.g.*, leak channels and fast outward currents), certain others will be out of phase (*e.g.*, fast calcium and sodium currents), and few others will be slow to rise and slow to fall (e.g., HCN). Thus, there will be different transmembrane currents associated with the same intracellular voltage response: some that are in phase with the voltage, some that are shifted by 90°, some at 180°, and others at arbitrary phases in between. The dominance of each of them vary with frequencies, implying that in some scenarios the capacitive current will be dominant whereas in others a specific ionic current might be dominant. Thus, the final phase of the total transmembrane current (with reference to the compartmental voltage) in each compartment would be variable depending on which component is dominant at the frequency at which the inputs arrive. Finally, as different compartments could be endowed with different densities of each ion channel, the phase of the extracellular potential recorded will be driven by the position of the recording electrodes (both extracellular and intracellular) as well. While each line current component will have a specific phase associated with the line segment being considered, the proximity of the extracellular electrode to a specific line segment as opposed to the others might enhance the contribution of that specific line segment. Similarly, as voltages within a cell also change with distance owing to RC filtering and other active filtering (Narayanan and Johnston, 2007, 2008; Vaidya and Johnston, 2013; Das et al., 2017), the position of the intracellular electrode plays a critical role in determining the phase difference between intra- and extra-cellular voltages.

With gap junctional inputs, a critical component that is absent is the 180° phase-shifted transmembrane synaptic current. The absence of this component results in strikingly different phase relationships between intra- and extra-cellular voltages in neurons receiving gap junctional inputs. Traditionally, the presence of gap junctions has been shown to enhance synchrony across neurons (Draguhn et al., 1998; Pfeuty et al., 2003). Our analyses provide evidence that the presence of gap junctional connectivity could redefine the relationship between extracellular potentials with intracellular voltages and spikes, apart from altering the polarity of extracellular signatures associated with synchronous inputs. The presence of gap junctions in oscillatory networks, such as interneuronal networks in the hippocampus that are implicated in the generation of gamma rhythms (Colgin, 2016), should be explicitly accounted for in computing and interpreting phase relationships between spikes and LFP oscillations.

Outward HCN currents regulate extracellular potentials.

An important observation from our analyses adds an intriguing facet to the multifarious physiology of HCN channels and their impact on local field potentials. There is sufficient evidence for a strong role of HCN channels in regulating local field potentials, given their subthreshold activation profile as well their slow gating kinetics (Sinha and Narayanan, 2015; Ness et al., 2016, 2018; Sinha and Narayanan, 2022). HCN channels conduct mixed cationic currents with a reversal potential of around $E_h = -30$ mV. They are activated by hyperpolarization and their conductance value (g_{HCN}) goes to zero at voltage values that are more depolarized than –50 mV (Robinson and Siegelbaum, 2003; Biel et al., 2009; Shah, 2014; Combe and Gasparini, 2021; Mishra and Narayanan, 2023). Thus, the current through HCN channels, $I_h = g_{\mathrm{HCN}}(V - E_h)$, has always been considered to be inward (negative in sign) in nature given that g_{HCN} falls to zero for positive values (when $V > E_h$) of the driving force $(V - E_h)$. In contrast to this traditional analyses associated with the polarity of HCN channels, our analyses provide two conditions under which HCN channels conduct outward currents, irrespective of whether inputs arrive through chemical synapses or gap junctions (Fig. 3; Supplementary Fig. S3).

First, the neuron should manifest a HCN conductance at resting membrane potential (RMP). Second, synaptic inputs should produce depolarizing responses that cross the reversal potential for HCN channels with fast kinetics. If these two conditions are met, then there is a duration where outward current flows through HCN channels, as a direct consequence of the slow deactivation kinetics of HCN channels. The first condition is easily met because most neurons that express HCN channels manifest a resting HCN conductance that is typically involved in regulating RMP. As

591 RMP is typically hyperpolarized compared to the reversal potential of HCN channels, the resting
592 current through HCN channels is inward in nature (Supplementary Fig. S3). The second
593 requirement is achievable if neurons receive synchronous inputs that are capable of driving the
594 membrane potentials to depolarized values beyond HCN channel reversal potential. Together, if the
595 kinetics of the voltage response is faster than the deactivation kinetics of HCN channels, an outward
596 current through HCN channels could manifest. This outward current could regulate intracellular
597 neuronal computations apart from contributing to extracellular potentials as observed in our
598 analyses. Strongly synchronous inputs are known to impinge on several neuronal subtypes
599 expressing HCN channels (Ariav et al., 2003; Bennett and Zukin, 2004; Diba et al., 2014; Connors,
600 2017). Therefore, future analyses involving HCN channels should account for the possibility of
601 outward HCN currents, both from the perspective of how they regulate cellular neurophysiology
602 and extracellular potentials.

603

604 **Limitations of analyses and future directions.**

605 Our analyses involved simulating a single morphologically and biophysically realistic neuronal
606 model with active dendrites. We chose this approach to delineate extracellular signatures associated
607 with the two types of synapses onto an individual neuron as well as to avoid the complexities
608 associated with cross-interactions of signals from multiple neurons (Geisler et al., 2010; Seenivasan
609 and Narayanan, 2020). However, LFPs are compound signals that involve several cross-interactions
610 across different cells of various subtypes, each receiving distinct patterns of inputs through different
611 types of synapses. Future studies should explore the implications of the stark differences between
612 extracellular signatures associated with gap junctional *vs*. chemical synaptic inputs in networks that
613 are endowed with different types of neurons connected through distinct synapse types.

614 As different neuronal subtypes are endowed with disparate sets of active dendritic
615 components, such analyses become essential in delineating the spatio-temporal and spectral
616 signatures of extracellular potentials associated with disparate inputs arriving at different parts of
617 the neuron (Colgin et al., 2009; Valero et al., 2015; Fernandez-Ruiz et al., 2017; Valero and de la
618 Prida, 2018; Navas-Olive et al., 2020; Mendoza-Halliday et al., 2024; Seenivasan et al., 2024).
619 Such analyses becomes especially essential in understanding cross-*strata* or cross-laminar
620 interactions between extracellular signals (simultaneously recorded within the same brain regions)
621 in disparate frequency bands (Colgin et al., 2009; Valero et al., 2015; Fernandez-Ruiz et al., 2017;
622 Valero and de la Prida, 2018; Navas-Olive et al., 2020; Mendoza-Halliday et al., 2024; Seenivasan
623 et al., 2024). LFP analyses could be assessed in the presence of several morphologically realistic

neuronal models, each receiving disparate patterns of inputs (Schomburg et al., 2012; Reimann et al., 2013; Sinha and Narayanan, 2015; Halnes et al., 2024), with details of gap junctional and chemical synaptic connectivity onto specific active dendritic structures within each subnetwork. Future analyses should also assess the impact of activity-dependent plasticity in ion channels (on dendrites, axonal initial segments, and other compartments), in synaptic receptors, and in gap junctions (Andersen et al., 2006; Johnston and Narayanan, 2008; Neves et al., 2008; O'Brien, 2014; Pereda, 2014; Coulon and Landisman, 2017; Magee and Grienberger, 2020; Mishra and Narayanan, 2021; Vaughn and Haas, 2022) on extracellular potentials with various kinds of inputs and different combinations of plasticity in various structures.

Our analyses focused on depolarizing synaptic currents, irrespective of whether they arrived through gap junctions or chemical synapses. Further analyses could focus on hyperpolarizing synaptic currents, especially assessing scenarios where both excitation and inhibition arrive onto active structures through chemical and/or electrical synapses. Several factors, including the spatiotemporal profile of excitation and inhibition arriving onto individual neurons, the type of synapses that excitatory and inhibitory inputs recruit, balance or lack thereof between excitatory and inhibitory inputs, and electrode localization would be crucial variables in shaping extracellular potentials in these analyses. Apart from synaptic subtype and active dendritic transmembrane currents which were the focus of this study, there are several other factors, including inhomogeneities in neuropil impedance profiles and ephaptic coupling, that contribute to shaping LFPs (Buzsaki et al., 2012; Einevoll et al., 2013; Sinha and Narayanan, 2022; Halnes et al., 2024).

METHODS

Pyramidal neuron model.

A multicompartmental, morphologically realistic, biophysical neuronal model for a CA1 pyramidal neuron was employed for all simulations. The 3D reconstruction of CA1 pyramidal neuron (*n123*) was taken from NeuroMorpho database (Ascoli et al., 2007). The models had detailed morphology with all parameters derived from electrophysiological data from pyramidal neurons of rat hippocampus. Active and passive mechanisms were incorporated into the model to match those of a CA1 pyramidal neuron, as detailed below.

Passive mechanisms.

The passive membrane properties were modeled as a combination of a capacitive current in parallel with a resistive current representing the leak channels. An axial resistivity parameter that accounted for intracellular resistance completed the passive representation of the neuronal model. Together, the parameters that defined the passive electrical properties of the neuron were: axial resistivity (R_a), specific membrane resistivity (R_m), and specific membrane capacitance (C_m). C_m and R_a were set to be uniform across the neuron at 1 μF/cm^2 and 120 Ω.cm, respectively. Specific membrane resistivity (R_m) varied nonuniformly in a sigmoidal manner (Golding et al., 2005; Narayanan and Johnston, 2007; Rathour and Narayanan, 2014; Basak and Narayanan, 2018) along the somatodendritic axis as a function of radial distance (x) of the compartments from soma:

$$R_m(x) = R_m^{soma} + \frac{R_m^{end} - R_m^{soma}}{1 + \exp\left(\frac{R_m^{hmp} - x}{R_m^{slope}}\right)} \qquad (1)$$

Descriptions of parameters and their default values are provided in Supplementary Table S1. The basal dendrites and axonal compartments had the same passive properties as the soma. The neuron was compartmentalized into 879 compartments using the d_λ rule (Carnevale and Hines, 2006), whereby each compartment was set to be smaller than 10% of λ_{100}, the space constant computed at 100 Hz. Out of these, there were 253 basal dendritic compartments.

Dynamics and distribution of active channels.

To model the active properties of the neuron, nine different types of ion channels were incorporated into the neuron model, based on electrophysiological characterization from CA1 pyramidal

neurons. Different types of ion channels were incorporated into active models: fast sodium (NaF), delayed rectifier potassium (KDR), hyperpolarization-activated cyclic nucleotide-gated non-specific cationic (HCN or *h*), *A*-type potassium (KA), *M*-type potassium (KM), *L*-type (CaL), *N*-type (CaN), *T*-type (CaT), and *R*-type (CaR) calcium channels. Current through Na, K, and HCN channels were modeled using an Ohmic formulation with the reversal potentials of Na^+, K^+, and HCN channels set at 55, –90, and –30 mV respectively. Current through calcium channels was modeled as per the Goldman-Hodgkin-Katz (GHK) conventions with the resting internal and external calcium concentration values set at 50 nM and 2 mM, respectively.

The conductances of NaF and KDR channels were set to be uniform across the somatodendritic arbor (Magee and Johnston, 1995; Hoffman et al., 1997). At the axonal initial segment (AIS), NaF density was tenfold higher and the conductance of KDR was double of its somatic counterpart. *N*-type calcium channels were uniformly distributed till 340 µm from soma along the apical dendrites (Magee and Johnston, 1995). *T*-type calcium channels were distributed with increasing density along the somatoapical axis as sigmoid gradient (Magee and Johnston, 1995), *M*-type potassium, and *L*-type calcium channels were distributed only at perisomatic regions till 50 µm from soma (Magee and Johnston, 1995; Hu et al., 2007). *R*-type calcium channels were distributed uniformly along somatodendritic arbor (Magee and Johnston, 1995). The gating properties and kinetics for these channels were derived from previous studies: NaF, KDR, and KA (Magee and Johnston, 1995; Hoffman et al., 1997; Migliore et al., 1999), HCN (Magee, 1998; Poolos et al., 2002), KM (Shah et al., 2008), CaT and CaN (Migliore et al., 1995), CaR and CaL (Magee and Johnston, 1995). The default conductance values associated with all ion channels are provided in Supplementary Table S1.

For KA channels, the differential kinetics and voltage-dependencies of the channel for proximal (radial distance, $x \leq 100$ µm from the soma) and distal ($x > 100$ µm from the soma) regions were accounted for (Hoffman et al., 1997; Migliore et al., 1999). The density of KA channel was set to increase linearly (Hoffman et al., 1997) as a function of distance of the dendritic compartment from soma (Supplementary Table S1):

$$g_{KA}(x) = g_{KA}^{soma}\left(1 + \frac{g_{KA}^{fold}}{100}x\right) \qquad (2)$$

The distribution and kinetics of HCN channels were adapted from previous studies of the hippocampal recordings for pyramidal neurons (Magee, 1998; Narayanan and Johnston, 2007). The kinetics and densities of HCN channels in basal dendrites were set the same as that of soma. The

gradient of maximal conductance of HCN followed a sigmoidal dependence along the radial distance, x, of the somatoapical arbor (Supplementary Table S1):

$$g_h(x) = \bar{g}_h \left(1 + \frac{g_h^{fold}}{1 + \exp\left(\frac{g_h^{hmp} - x}{g_h^{slope}} \right)} \right) \quad (3)$$

For apical dendrites, the conductance of the *T*-type calcium (CaT) channels was set to increase with radial distance as a sigmoid function (Supplementary Table S1):

$$g_{CaT}(x) = \bar{g}_{CaT} \left(1 + \frac{g_{CaT}^{fold}}{1 + \exp\left(\frac{g_{CaT}^{hmp} - x}{g_{CaT}^{slope}} \right)} \right) \quad (4)$$

The CaT conductance for basal dendritic compartment were set to be the same as that of the soma.

Models and virtual knockouts.

To understand the contribution of different active dendritic transmembrane currents on extracellular potentials, we compared active (with all active conductances intact) and passive (leak channels were the only ion channels present) in the dendrites of these models. Note that in passive dendritic models, the soma continued to be active to accommodate action potential generation. For the models labeled "No sodium" and "No leak", the sodium conductance and leak conductance were set to zero, respectively, throughout the neuron (including the soma). For the knockout model labeled "No sodium or leak", both sodium and leak channel conductance values were set to zero across the neuron (including the soma).

Chemical synaptic and gap junctional inputs: Characteristics and temporal dynamics.

We employed excitatory chemical synapses (default number=245) which were randomly dispersed across the basal dendritic tree by picking locations from a uniform distribution of indexed locations. Synaptic receptors were modeled using a two-exponential formulation (Carnevale and Hines, 2006), with rise time constant (τ_r) and decay time constant (τ_d) set at 5 ms and 25 ms, respectively. The reversal potential for excitatory synaptic currents was 0 mV, and the default peak conductance was set to 150 pS. The time of activation of a chemical synapse refers to the time at which the

postsynaptic conductance associated with that synapse changes towards initiating the two-exponential dynamics.

For modeling electrical synapses (Supplementary Fig. S1), membrane potential deflections from different locations were recorded from other simulated neurons (which represented the other neurons connecting through gap junctions) that received chemical synaptic inputs. The chemical synapses onto these other neurons and their dendritic distribution were modeled in similar fashion as described above. The recorded voltage waveforms from different compartments of these other neurons were differently shaped, as post-synaptic potentials or as action potentials or as dendritic spikes (Supplementary Fig. S1). These recorded voltage waveforms were normalized, converted to currents, scaled using a scaling factor, and directly injected as currents of the same sign into locations where the designated gap junctions were placed (Supplementary Fig. S1). A default number of ninety-nine randomly dispersed gap junctional inputs were placed on basal dendritic locations of the neuron under consideration. The specific waveform (from the several recorded ones) associated with each of the 99 gap junctional inputs was randomized across trials and dendritic locations. Injected current was scaled such that they generated local responses of ≤ 5 mV amplitude. Across different locations, scaling factor values ranged between 0.05–0.405 for models with active dendrites and between 0.009–0.3645 models with passive dendrites. The time of activation of a gap junction refers to the start time at which the associated current waveform was injected into the compartment where the gap junction was placed.

The precise nature of LFPs depends on spatial localization of synapses, the transmembrane currents from active structures, and on the temporal patterns of impinging activity (Buzsaki et al., 2012; Einevoll et al., 2013; Sinha and Narayanan, 2022). To assess the impact of different temporal patterns of activity on LFPs, chemical or electrical synapses were activated with three distinct temporal patterns of activity: synchronous, random, and rhythmic inputs. As the goal of this study was to assess differences in extracellular signatures associated with chemical synapses *vs*. gap junctions, the neuronal model under consideration received inputs exclusively either through chemical synapses or through gap junctions. There were no models that received both chemical synaptic as well as gap junctional inputs.

Synchronous synaptic inputs.

Synchronous inputs were temporally synchronized excitatory inputs onto the dendrites, which are known to induce high-precision firing responses in the postsynaptic neurons (Ariav et al., 2003).

All models used for the simulation with synchronous inputs were tuned to obtain only one action potential for the ease of quantitatively delineating the associated extracellular potentials. In achieving this for models with chemical synapses, the maximal sodium conductance, $\bar{g}_{Na}$ set to a default value of 30 mS/cm^2 and maximal delayed rectifier potassium channel conductance, $\bar{g}_{KDR}$was 32 mS/cm^2. For the models with gap junctions, the default values for $\bar{g}_{Na}$was set to 26 mS/cm^2 and $\bar{g}_{KDR}$ was set at 8 mS/cm^2.

Random synaptic inputs.

Neuronal dendrites could receive asynchronous afferents from other brain regions. We performed simulations with random asynchronous inputs that activated the neuron independently, either through chemical synapses or gap junctions. These asynchronous inputs arrived onto their targets at low- or high-frequency and were named as low-frequency random inputs (LFRI) and high-frequency random inputs (HFRI), respectively. All synapses in the group were randomly activated within a 410.5 ms window for LFRI and within a 52.45 ms window for HFRI.

Rhythmic synaptic inputs.

Several neurons receive patterned inputs at different frequencies which yield distinct output patterns in neuronal responses (Buzsaki, 2006; Colgin, 2016). We introduced rhythmic excitatory afferent inputs at eight different frequencies: 1, 2, 4, 8, 16, 32, 64, and 128 Hz, designed to span most rhythms of the brain. Each simulation consisted of ten temporal cycles with each cycle activating 500 random locations at basal dendrites. These patterned stimuli impinged onto neurons either through chemical synapses or gap junctions. Rhythmic synaptic inputs were presented as a periodically Gaussian activation pattern with a period set at $1/f$ s and SD of $0.25/f$ s, where f was one of the eight frequencies above (Schomburg et al., 2012; Sinha and Narayanan, 2015).

For simulations involving these three different kinds of temporal patterns of inputs, intracellular potentials and transmembrane currents from individual dendritic compartments were recorded and were used for further analyses.

Positioning of extracellular electrodes and computation of extracellular potentials.

We employed seven arrays of virtual electrodes, with each array made of 49 (7 × 7) electrodes, giving a total of 343 electrodes in a 7 × 7 × 7 cubic organization. These electrodes were placed over

basal dendrites spanning the region from soma to the terminal end of the basal dendrites. The inter-electrode distance for each of the 3 axes was approximately 35 μm. For plotting and analysis purposes, EFP recordings from each of these electrodes were binned into 10 groups depending on their radial distance from the soma (Supplementary Table S2).

Extracellular potentials were recorded from each of these 343 electrodes as distance-scaled summation of line-source approximated currents from all line segments in the morphological realistic neuron. For each electrode, the extracellular voltage was computed as (Rall and Shepherd, 1968; Holt and Koch, 1999; Gold et al., 2006; Linden et al., 2010; Linden et al., 2011; Buzsaki et al., 2012; Schomburg et al., 2012; Einevoll et al., 2013; Linden et al., 2013; Reimann et al., 2013; Sinha and Narayanan, 2015, 2022):

$$V_{\text{ext}}(t) = \frac{1}{4\pi\sigma}\sum_{n=1}^{N}\frac{I_n(t)}{L_n}\log\frac{\sqrt{h_n^2 + r_n^2} - h_n}{\sqrt{s_n^2 + r_n^2} - s_n} \qquad (5)$$

where σ defined the uniform conductivity of the extracellular medium (default value: 0.3 S/m), I_n represented the line current associated with line source n. L_n was the length of the line segment. h_n, r_n, and s_n defined geometry-related parameters that were dependent on the specific pair of electrode and line segment. r_n was the perpendicular distance from the electrode to a line through the compartment, h_n represented the longitudinal separation along this line from the electrode to one end of the compartment, and s_n was computed as the sum of h_n and L_n. As the default integration time constant for obtaining the transmembrane currents was 25 μs, the sampling rate for $I_{\text{n}}(t)$ and $V_{\text{ext}}(t)$ was 40 kHz.

Analysis of extracellular field potentials.

Extracellular potentials recorded from all the electrodes were bandpass filtered with lower frequency cutoff of 0.5 Hz and higher frequency limit of 300 Hz to obtain local field potentials (LFPs) for that electrode. Filtering was implemented using a zero-phase, second-order, bandpass Butterworth filter on signals sampled at 40 kHz. With the synchronous stimulation paradigm, peak-to-peak field potential value were measured as the difference between peak positive and peak negative LFP deflections (within an 85-ms window after stimulation) for each electrode. The peak positive and the peak negative deflections were also computed separately for each electrode. For the random stimulation paradigm, LFPs associated with chemical *vs*. electrical stimulation were compared by computing the Fourier transform of the LFP waveform as well as the spectrogram of the LFP waveform using wavelet transform. For rhythmic synaptic inputs, each of the eight

different frequency inputs (1, 2, 4, 8, 16, 32, 64, and 128 Hz) were filtered in specific bandpass frequency cut-off for higher and lower limits (Supplementary Table S3) using a zero-phase, second order (for all frequencies except for the 1 Hz, where the order was one) Butterworth filter. Peak power was obtained from the Fourier power spectrum associated with the EFP from each of the electrodes.

Computing phase of spikes with respect to LFP oscillations associated with rhythmic synaptic inputs.

For assessing spike phases associated with rhythmic synaptic inputs (at each of the 8 frequencies mentioned above), we first tuned the model using a range of synaptic weights or scaling factor for synaptic and junctional inputs, respectively, towards eliciting a single spike per oscillatory cycle. These simulations were performed over five trials, with trials differing in synaptic locations and specific inputs to these synapses. An example of parameters used in a trial of synaptic and junctional inputs are shown in Supplementary Tables S4–S5, respectively. The timing of spikes, in cycles that the neuron spiked, were recorded from soma. Extracellular potentials recorded from the electrode nearest to the soma (located 14.11 μm away from soma) was used for deriving LFPs. Extracellular potentials were filtered based on oscillatory frequency that the patterned inputs were presented through gap junctions or chemical synapses.

To assign the phase of spike in relation to LFP oscillations, the troughs from each oscillatory cycle were identified by locating the minima of field potentials for respective cycle (Seenivasan and Narayanan, 2020). The troughs were designated a phase of 0°. The phases of individual spikes were computed with reference to the troughs that preceded and followed the spike. To elaborate, let's consider t_{spike} as the timing of a spike elicited in response to the patterned inputs. For each spike (t_{spike}), two troughs from the cycles were considered: one occurring just before t_{spike} (t_L), and another immediately after t_{spike} (t_R). Thus, the spike under consideration occurred between these two consecutive troughs which are separated by a phase of 360°. Therefore, phase of the spike (ϕ_{spike}, in degrees) with reference to the oscillatory LFP was calculated as (Seenivasan and Narayanan, 2020):

$$\phi_{spike} = 360 \times \frac{t_{spike} - t_L}{t_R - t_L} \qquad (6)$$

This computation was executed for all the spikes elicited by neuron in respective oscillatory cycles across all trials to assess spike phases with reference to the respective LFP oscillatory patterns.

Computing phase of intracellular voltages with respect to LFP in models receiving rhythmic inputs.

With reference to rhythmic synaptic inputs at each of the 8 frequencies mentioned above, to examine the phase of intracellular voltage traces in relation to the corresponding LFP oscillations, cross-correlation between these two waveforms was computed. To investigate the contribution of sodium conductances, we conducted cross-correlation simulations for two scenarios: one involving intracellular somatic voltages in the presence of sodium channels, filtered at respective frequencies, and another where the sodium conductance was set to zero. Parameters used for executing cross-correlation between field and somatic potentials without sodium conductance are shown in Supplementary Tables S6–S7 for synaptic and junctional inputs, respectively. Extracellular potentials were individually computed for each scenario (with sodium and no sodium) and used for cross-correlation analysis with the respective somatic voltage waveforms.

Cross-correlation was computed between the time series of soma-adjacent LFP and the associated somatic voltage. The lag (τ) corresponding to the maximum correlation was computed, and $T\ (= 1/f)$ represented the time-period of the respective oscillation. The phase difference between the intracellular and extracellular waveforms (ϕ_{IE}, in degrees) was calculated as:

$$\phi_{IE} = 360 \times \frac{\tau}{T} \tag{7}$$

Computational details.

Morphological and biophysical properties of CA1 neuron model along with synapses, and intracellular simulations were performed using custom-written codes in the NEURON simulation environment (Carnevale and Hines, 2006). The computation of extracellular field potentials was performed using LFPy (Linden et al., 2013; Halnes et al., 2024) interfaced with NEURON (Carnevale and Hines, 2006) through Python. LFPy simulations were performed in Jupyter python terminal (https://jupyter.org) using custom-written python codes. All simulations were performed with resting membrane potential of neuron model set at -65mV and the temperature set to 34º C. The integration time step was fixed to 25 µs. Coordinates for the electrodes 3D positioning spanning dendrites were obtained using MATLAB R2015b (Mathworks). Data analyses were done using MATLAB or custom-built software written in IGOR Pro programming environment (Wavemetrics).

Statistical analyses.

All statistical analyses were performed using R statistical package (www.r-project.org). We performed Wilcoxon rank-sum test for comparing distribution of LFP data from active and passive models. In these, variability in data is shown as median with quartile. *p* values for each statistical test are provided in the figure legends associated with the specific figure panels.

REFERENCES

Alvarez VA, Chow CC, Van Bockstaele EJ, Williams JT (2002) Frequency-dependent synchrony in locus ceruleus: role of electrotonic coupling. Proc Natl Acad Sci U S A 99:4032-4036.

Anastassiou CA, Perin R, Buzsaki G, Markram H, Koch C (2015) Cell type- and activity-dependent extracellular correlates of intracellular spiking. Journal of neurophysiology 114:608-623.

Andersen P, Morris R, Amaral D, Bliss T, O'Keefe J (2006) The hippocampus book. New York, USA: Oxford University Press.

Ariav G, Polsky A, Schiller J (2003) Submillisecond precision of the input-output transformation function mediated by fast sodium dendritic spikes in basal dendrites of CA1 pyramidal neurons. J Neurosci 23:7750-7758.

Ascoli GA, Donohue DE, Halavi M (2007) NeuroMorpho.Org: a central resource for neuronal morphologies. J Neurosci 27:9247-9251.

Basak R, Narayanan R (2018) Spatially dispersed synapses yield sharply-tuned place cell responses through dendritic spike initiation. J Physiol 596:4173-4205.

Bennett MV, Zukin RS (2004) Electrical coupling and neuronal synchronization in the Mammalian brain. Neuron 41:495-511.

Biel M, Wahl-Schott C, Michalakis S, Zong X (2009) Hyperpolarization-activated cation channels: from genes to function. Physiol Rev 89:847-885.

Bullock TH (1951) Conduction and transmission of nerve impulses. Annual review of physiology 13:261-280.

Buzsaki G (2004) Large-scale recording of neuronal ensembles. Nat Neurosci 7:446-451.

Buzsaki G (2006) Rhythms of the brain. New York: Oxford University Press.

Buzsaki G, Anastassiou CA, Koch C (2012) The origin of extracellular fields and currents--EEG, ECoG, LFP and spikes. Nature reviews Neuroscience 13:407-420.

Carnevale NT, Hines ML (2006) The NEURON Book. Cambridge, UK: Cambridge University Press.

Christie MJ, Williams JT, North RA (1989) Electrical coupling synchronizes subthreshold activity in locus coeruleus neurons in vitro from neonatal rats. J Neurosci 9:3584-3589.

Colgin LL (2016) Rhythms of the hippocampal network. Nature reviews Neuroscience 17:239-249.

Colgin LL, Denninger T, Fyhn M, Hafting T, Bonnevie T, Jensen O, Moser MB, Moser EI (2009) Frequency of gamma oscillations routes flow of information in the hippocampus. Nature 462:353-357.

Combe CL, Gasparini S (2021) I(h) from synapses to networks: HCN channel functions and modulation in neurons. Prog Biophys Mol Biol 166:119-132.

Connors BW (2017) Synchrony and so much more: Diverse roles for electrical synapses in neural circuits. Dev Neurobiol 77:610-624.

Connors BW, Long MA (2004) Electrical synapses in the mammalian brain. Annu Rev Neurosci 27:393-418.

Coulon P, Landisman CE (2017) The Potential Role of Gap Junctional Plasticity in the Regulation of State. Neuron 93:1275-1295.

Curtis HJ, Travis DM (1951) Conduction in Purkinje tissue of the ox heart. Am J Physiol 165:173-178.

Dale H (1934) Chemical Transmission of the Effects of Nerve Impulses. Br Med J 1:835-841.

Das A, Rathour RK, Narayanan R (2017) Strings on a Violin: Location Dependence of Frequency Tuning in Active Dendrites. Front Cell Neurosci 11:72.

Diba K, Amarasingham A, Mizuseki K, Buzsaki G (2014) Millisecond timescale synchrony among hippocampal neurons. J Neurosci 34:14984-14994.

Draguhn A, Traub RD, Schmitz D, Jefferys JG (1998) Electrical coupling underlies high-frequency oscillations in the hippocampus in vitro. Nature 394:189-192.
Einevoll GT, Kayser C, Logothetis NK, Panzeri S (2013) Modelling and analysis of local field potentials for studying the function of cortical circuits. Nature reviews Neuroscience 14:770-785.
Fernandez-Ruiz A, Oliva A, Nagy GA, Maurer AP, Berenyi A, Buzsaki G (2017) Entorhinal-CA3 Dual-Input Control of Spike Timing in the Hippocampus by Theta-Gamma Coupling. Neuron 93:1213-1226 e1215.
Furshpan EJ, Potter DD (1957) Mechanism of nerve-impulse transmission at a crayfish synapse. Nature 180:342-343.
Geisler C, Diba K, Pastalkova E, Mizuseki K, Royer S, Buzsaki G (2010) Temporal delays among place cells determine the frequency of population theta oscillations in the hippocampus. Proc Natl Acad Sci U S A 107:7957-7962.
Gold C, Henze DA, Koch C, Buzsaki G (2006) On the origin of the extracellular action potential waveform: A modeling study. Journal of neurophysiology 95:3113-3128.
Golding NL, Mickus TJ, Katz Y, Kath WL, Spruston N (2005) Factors mediating powerful voltage attenuation along CA1 pyramidal neuron dendrites. J Physiol 568:69-82.
Halnes G, Ness TV, Næss S, Hagen E, Pettersen KH, Einevoll GT (2024) Electric Brain Signals: Foundations and Applications of Biophysical Modeling. Cambridge: Cambridge University Press.
Hamzei-Sichani F, Davidson KG, Yasumura T, Janssen WG, Wearne SL, Hof PR, Traub RD, Gutierrez R, Ottersen OP, Rash JE (2012) Mixed Electrical-Chemical Synapses in Adult Rat Hippocampus are Primarily Glutamatergic and Coupled by Connexin-36. Frontiers in neuroanatomy 6:13.
Hoffman DA, Magee JC, Colbert CM, Johnston D (1997) K+ channel regulation of signal propagation in dendrites of hippocampal pyramidal neurons. Nature 387:869-875.
Holt GR, Koch C (1999) Electrical interactions via the extracellular potential near cell bodies. J Comput Neurosci 6:169-184.
Hu H, Vervaeke K, Storm JF (2007) M-channels (Kv7/KCNQ channels) that regulate synaptic integration, excitability, and spike pattern of CA1 pyramidal cells are located in the perisomatic region. J Neurosci 27:1853-1867.
Johnston D, Narayanan R (2008) Active dendrites: colorful wings of the mysterious butterflies. Trends Neurosci 31:309-316.
Kepler TB, Marder E, Abbott LF (1990) The effect of electrical coupling on the frequency of model neuronal oscillators. Science 248:83-85.
Kopell N, Ermentrout B (2004) Chemical and electrical synapses perform complementary roles in the synchronization of interneuronal networks. Proc Natl Acad Sci U S A 101:15482-15487.
Lebedev MA, Nicolelis MA (2017) Brain-Machine Interfaces: From Basic Science to Neuroprostheses and Neurorehabilitation. Physiol Rev 97:767-837.
Linden H, Pettersen KH, Einevoll GT (2010) Intrinsic dendritic filtering gives low-pass power spectra of local field potentials. J Comput Neurosci 29:423-444.
Linden H, Hagen E, Leski S, Norheim ES, Pettersen KH, Einevoll GT (2013) LFPy: a tool for biophysical simulation of extracellular potentials generated by detailed model neurons. Frontiers in neuroinformatics 7:41.
Linden H, Tetzlaff T, Potjans TC, Pettersen KH, Grun S, Diesmann M, Einevoll GT (2011) Modeling the spatial reach of the LFP. Neuron 72:859-872.
Loewi O (1945) Chemical transmission of nerve impulses. American Scientist 33:159-174.
Magee JC (1998) Dendritic hyperpolarization-activated currents modify the integrative properties of hippocampal CA1 pyramidal neurons. J Neurosci 18:7613-7624.

Magee JC, Johnston D (1995) Characterization of single voltage-gated Na+ and Ca2+ channels in apical dendrites of rat CA1 pyramidal neurons. J Physiol 487:67-90.
Magee JC, Grienberger C (2020) Synaptic Plasticity Forms and Functions. Annu Rev Neurosci 43:95-117.
Major G, Larkum ME, Schiller J (2013) Active properties of neocortical pyramidal neuron dendrites. Annu Rev Neurosci 36:1-24.
Mendoza-Halliday D, Major AJ, Lee N, Lichtenfeld MJ, Carlson B, Mitchell B, Meng PD, Xiong YS, Westerberg JA, Jia X, Johnston KD, Selvanayagam J, Everling S, Maier A, Desimone R, Miller EK, Bastos AM (2024) A ubiquitous spectrolaminar motif of local field potential power across the primate cortex. Nat Neurosci 27:547-560.
Migliore M, Hoffman DA, Magee JC, Johnston D (1999) Role of an A-type K+ conductance in the back-propagation of action potentials in the dendrites of hippocampal pyramidal neurons. J Comput Neurosci 7:5-15.
Migliore M, Cook EP, Jaffe DB, Turner DA, Johnston D (1995) Computer simulations of morphologically reconstructed CA3 hippocampal neurons. Journal of neurophysiology 73:1157-1168.
Mishra P, Narayanan R (2021) Stable continual learning through structured multiscale plasticity manifolds. Current opinion in neurobiology 70:51-63.
Mishra P, Narayanan R (2023) The enigmatic HCN channels: A cellular neurophysiology perspective. Proteins.
Nagy JI, Pereda AE, Rash JE (2018) Electrical synapses in mammalian CNS: Past eras, present focus and future directions. Biochim Biophys Acta Biomembr 1860:102-123.
Nagy JI, Pereda AE, Rash JE (2019) On the occurrence and enigmatic functions of mixed (chemical plus electrical) synapses in the mammalian CNS. Neuroscience letters 695:53-64.
Narayanan R, Johnston D (2007) Long-term potentiation in rat hippocampal neurons is accompanied by spatially widespread changes in intrinsic oscillatory dynamics and excitability. Neuron 56:1061-1075.
Narayanan R, Johnston D (2008) The h channel mediates location dependence and plasticity of intrinsic phase response in rat hippocampal neurons. J Neurosci 28:5846-5860.
Navas-Olive A, Valero M, Jurado-Parras T, de Salas-Quiroga A, Averkin RG, Gambino G, Cid E, de la Prida LM (2020) Multimodal determinants of phase-locked dynamics across deep-superficial hippocampal sublayers during theta oscillations. Nature communications 11:2217.
Ness TV, Remme MWH, Einevoll GT (2016) Active subthreshold dendritic conductances shape the local field potential. J Physiol 594:3809-3825.
Ness TV, Remme MWH, Einevoll GT (2018) h-Type Membrane Current Shapes the Local Field Potential from Populations of Pyramidal Neurons. J Neurosci 38:6011-6024.
Neves G, Cooke SF, Bliss TV (2008) Synaptic plasticity, memory and the hippocampus: a neural network approach to causality. Nature reviews Neuroscience 9:65-75.
O'Brien J (2014) The ever-changing electrical synapse. Current opinion in neurobiology 29:64-72.
Obien ME, Deligkaris K, Bullmann T, Bakkum DJ, Frey U (2014) Revealing neuronal function through microelectrode array recordings. Front Neurosci 8:423.
Pandarinath C, Bensmaia SJ (2022) The science and engineering behind sensitized brain-controlled bionic hands. Physiol Rev 102:551-604.
Pereda AE (2014) Electrical synapses and their functional interactions with chemical synapses. Nature reviews Neuroscience 15:250-263.

Pesaran B, Vinck M, Einevoll GT, Sirota A, Fries P, Siegel M, Truccolo W, Schroeder CE, Srinivasan R (2018) Investigating large-scale brain dynamics using field potential recordings: analysis and interpretation. Nat Neurosci 21:903-919.
Pfeuty B, Mato G, Golomb D, Hansel D (2003) Electrical synapses and synchrony: the role of intrinsic currents. J Neurosci 23:6280-6294.
Poolos N, Migliore M, Johnston D (2002) Pharmacological upregulation of h-channels reduces the excitability of pyramidal neuron dendrites. Nat Neurosci 5:767-774.
Rall W, Shepherd GM (1968) Theoretical reconstruction of field potentials and dendrodendritic synaptic interactions in olfactory bulb. Journal of neurophysiology 31:884-915.
Rathour RK, Narayanan R (2014) Homeostasis of functional maps in active dendrites emerges in the absence of individual channelostasis. Proc Natl Acad Sci U S A 111:E1787-1796.
Reimann MW, Anastassiou CA, Perin R, Hill SL, Markram H, Koch C (2013) A biophysically detailed model of neocortical local field potentials predicts the critical role of active membrane currents. Neuron 79:375-390.
Robinson RB, Siegelbaum SA (2003) Hyperpolarization-activated cation currents: from molecules to physiological function. Annual review of physiology 65:453-480.
Schomburg EW, Anastassiou CA, Buzsaki G, Koch C (2012) The spiking component of oscillatory extracellular potentials in the rat hippocampus. J Neurosci 32:11798-11811.
Seenivasan P, Narayanan R (2020) Efficient phase coding in hippocampal place cells. Physical Review Research 2:033393.
Seenivasan P, Basak R, Narayanan R (2024) Cross-strata co-occurrence of ripples with theta-frequency oscillations in the hippocampus of foraging rats. J Physiol 602:2315-2341.
Shah MM (2014) Cortical HCN channels: function, trafficking and plasticity. J Physiol 592:2711-2719.
Shah MM, Migliore M, Valencia I, Cooper EC, Brown DA (2008) Functional significance of axonal Kv7 channels in hippocampal pyramidal neurons. Proc Natl Acad Sci U S A 105:7869-7874.
Sherman A, Rinzel J (1992) Rhythmogenic effects of weak electrotonic coupling in neuronal models. Proc Natl Acad Sci U S A 89:2471-2474.
Sinha M, Narayanan R (2015) HCN channels enhance spike phase coherence and regulate the phase of spikes and LFPs in the theta-frequency range. Proc Natl Acad Sci U S A 112:E2207-2216.
Sinha M, Narayanan R (2022) Active Dendrites and Local Field Potentials: Biophysical Mechanisms and Computational Explorations. Neuroscience 489:111-142.
Skinner FK, Zhang L, Velazquez JL, Carlen PL (1999) Bursting in inhibitory interneuronal networks: A role for gap-junctional coupling. Journal of neurophysiology 81:1274-1283.
Sohl G, Maxeiner S, Willecke K (2005) Expression and functions of neuronal gap junctions. Nature reviews Neuroscience 6:191-200.
Stuart GJ, Spruston N (2015) Dendritic integration: 60 years of progress. Nat Neurosci 18:1713-1721.
Traub RD (1995) Model of synchronized population bursts in electrically coupled interneurons containing active dendritic conductances. J Comput Neurosci 2:283-289.
Traub RD, Bibbig A (2000) A model of high-frequency ripples in the hippocampus based on synaptic coupling plus axon-axon gap junctions between pyramidal neurons. J Neurosci 20:2086-2093.
Traub RD, Cunningham MO, Whittington MA (2011) Chemical synaptic and gap junctional interactions between principal neurons: partners in epileptogenesis. Neural Netw 24:515-525.

Traub RD, Whittington MA, Gutierrez R, Draguhn A (2018) Electrical coupling between hippocampal neurons: contrasting roles of principal cell gap junctions and interneuron gap junctions. Cell Tissue Res 373:671-691.

Traub RD, Schmitz D, Maier N, Whittington MA, Draguhn A (2012) Axonal properties determine somatic firing in a model of in vitro CA1 hippocampal sharp wave/ripples and persistent gamma oscillations. The European journal of neuroscience 36:2650-2660.

Traub RD, Pais I, Bibbig A, LeBeau FE, Buhl EH, Hormuzdi SG, Monyer H, Whittington MA (2003) Contrasting roles of axonal (pyramidal cell) and dendritic (interneuron) electrical coupling in the generation of neuronal network oscillations. Proc Natl Acad Sci U S A 100:1370-1374.

Vaidya SP, Johnston D (2013) Temporal synchrony and gamma-to-theta power conversion in the dendrites of CA1 pyramidal neurons. Nat Neurosci 16:1812-1820.

Valero M, de la Prida LM (2018) The hippocampus in depth: a sublayer-specific perspective of entorhinal-hippocampal function. Current opinion in neurobiology 52:107-114.

Valero M, Cid E, Averkin RG, Aguilar J, Sanchez-Aguilera A, Viney TJ, Gomez-Dominguez D, Bellistri E, de la Prida LM (2015) Determinants of different deep and superficial CA1 pyramidal cell dynamics during sharp-wave ripples. Nat Neurosci 18:1281-1290.

Vaughn MJ, Haas JS (2022) On the Diverse Functions of Electrical Synapses. Front Cell Neurosci 16:910015.

Verkhratsky A, Nedergaard M (2018) Physiology of Astroglia. Physiol Rev 98:239-389.

Watanabe A (1958) The interaction of electrical activity among neurons of lobster cardiac ganglion. The Japanese journal of physiology 8:305-318.

ACKNOWLEDGMENTS

The authors thank members of the cellular neurophysiology laboratory for helpful discussions and for comments on a draft of this manuscript.

Funding: This work was supported by:

- Wellcome Trust-DBT India Alliance (Senior fellowship to R. N.; IA/S/16/2/502727)
- Ministry of education (Scholarship funds to R.S.; Research funds to R. N.).

Author contributions:

Conceptualization: RS, RN
Methodology: RS
Investigation: RS
Visualization: RS
Supervision: RS, RN
Writing—original draft: RS
Writing—review & editing: RS, RN

Competing interests: Authors declare that they have no competing interests.

Data and materials availability: All data are available in the main text or the supplementary materials.

SUPPLEMENTARY INFORMATION

A supplementary file containing 11 supplementary figures and 7 supplementary tables is being uploaded.